Capacitive Micromachined Ultrasound Transducers for Non-Destructive Testing Applications

by

Tirad Owais

A thesis
presented to the University of Waterloo
in fulfillment of the
thesis requirement for the degree of
Master of Applied Science
in
Mechanical and Mechatronics Engineering

Waterloo, Ontario, Canada, 2020

© Tirad Owais 2020

Author's Declaration

I hereby declare that I am the sole author of this thesis. This is a true copy of the thesis, including any required final revisions, as accepted by my examiners.

I understand that my thesis may be made electronically available to the public.

Abstract

The need for using ultrasound non-destructive testing (NDT) to characterize, test and detect flaws within metals, led us to utilize Capacitive Micromachined Ultrasound Transducers (CMUTs) in the ultrasound NDT field. This is due to CMUT's large bandwidths and high receive sensitivity, to be a suitable substitute for piezoelectric (PZT) transducers in NDT applications.

The basic operational test of CMUTs, conducted in this research, was carried out based on a pulse-echo technique by propagating acoustic pulses into an object and analyzing the reflected signals. Thus, characterizing the tested material, measuring its dimension, and detecting flaws within it can be achieved.

Throughout the course of this research, the fundamental parameters of CMUT including pull-in voltage and resonance frequency were initially calculated analytically and using Finite Element Analysis (FEA). Afterward, the CMUT was fabricated out of two mechanically bonded wafers. The device's movable membrane (top electrode) and stationary electrode (bottom electrode) were made out of Boron-doped Silicon. The two electrodes were electrically isolated by an insulation layer containing a sealed gap.

The CMUT was then tested and characterized to analyze its performance for NDT applications. In-immersion characterization revealed that the 2.22 MHz CMUT obtained a -6 dB fractional bandwidth of 189%, and a receive sensitivity of 31.15 mV/kPa, compared to 45% and 4.83 mV/kPa of the PZT probe. A pulse-echo test, performed to examine an aluminum block with and without flaws, showed success in distinguishing the surfaces and the flaws of the tested sample.

Acknowledgements

Foremost, all praises be to Allah for bestowing his dense blessings, true guidence and endless help. Following, I would like to wholeheartedly appreciate my parents and my siblings for their unconditional help and support throughout my entire life; without them, traveling this far road would have been impossible.

I offer my enduring gratitude to my supervisor, at the University of Waterloo, Prof. John Yeow for the true guidance, inspiration, and endless support, financially and academically, throughout my Master's study. I would like to wholeheartedly thank him for giving me the opportunity to work and live the experience in the microelectromechanical (MEMS) world with many friends under the ceiling of his Advanced Micro-/Nano- Devices Lab (AMNDL). A special gratitude to my labmate Dr. Zhou Zheng (Joe) for providing me a plenty of his knowledge about CMUT technology. I am especially thankful to my close friend Dr. Ayman Alneamy for his constant help and profound insight about MEMS world and answering all the questions I had in that regard. Also a special thanks to Prof. Eihab Abdel-Rahman for giving me the opportunity to use the vibrometer equipment in his lab. This work will not be possible without the financial supports from the CMC Microsystem.

Lastly, and most specially, I would like to thank my beloved wife, Waad, and my beloved daughters, Hala and Joud. Thanks to the best wife for sharing most precious time in her life with me and being consistently patient, supportive, and understanding during my study period.

This work was financially and academically supported by Prince Sattam bin Abdulaziz University (PSAU), Saudi Arabia.

Dedication

To my parents,

To my brothers,

To my sisters,

To my beloved wife, and daughters.

Who have always been there for me, and to whom I owe everything that I have achieved!

with respect and love!

Table of Contents

Author's Declaration .... **ii**

Abstract .... **iii**

Acknowledgements .... **iv**

Dedication .... **v**

List of Figures .... **viii**

List of Tables .... **xi**

List of Abbreviations .... **xii**

List of Nomenclatures .... **xiv**

Chapter 1 Introduction **1**

1.1 Motivations 1

1.2 Background on Ultrasound 4

1.3 Background on CMUT 7

Chapter 2 Modeling of CMUT **10**

2.1 Analytical Modeling 12

2.1.1 Pull-in Voltage 15

2.1.2 Resonance Frequency 18

2.2 Finite Element Analysis 20

2.2.1 CMUT Model Set-up 21

2.2.2 Eigen Frequency Analysis and Frequency Response 22

2.2.3 Pull-in Voltage Phenomenon 25

Chapter 3 CMUT Fabrication 27

3.1 Surface Micromachining Process 27

3.2 Wafer Bonding Process 29

3.2.1 Photolithography Process 33

Chapter 4 CMUT Testing and Characterization 36

4.1 Air-coupled Characterization 36

4.1.1 Dynamic Analysis 38

4.2 In-immersion Testing and Characterization 42

4.2.1 PZT and CMUT Transmission Tests 43

4.2.2 PZT and CMUT Reception Tests 46

4.2.3 CMUT Pulse-echo Tests 49

Chapter 5 Summary and Future Work 54

5.1 Summary 54

5.2 Future Work 55

Bibliography 57

Appendices 65

Appendix-Images of CMUT Masking Layouts and Fabricated Device........................65

List of Figures

Figure 1.1: Relationship between the penetration depth and the image resolution as a function of operational frequency [42]..3

Figure 1.2: A simple pulse-echo test for defined flaw boundary of a material [34]................ 5

Figure 1.3: Acoustic propagation at the interface of two media... 6

Figure 1.4: A pulse-echo event in the time domain.. 7

Figure 1.5: PZT Transducer probe structural overview.. 8

Figure 1.6: Cross-section of a basic unit of a CMUT.. 9

Figure 2.1: CMUT mass-spring-damper system... 12

Figure 2.2: (a) Center membrane deflection of a CMUT unit cell, (b) Equivalent plate shape of a circular CMUT membrane... 13

Figure 2.3: Membrane displacement vs. DC bias voltage, showing the pull-in phenomenon... 16

Figure 2.4: The relationship between electrostatic force and spring force vs. gap distance as a function of DC bias voltage when $Vdc<Vpull\text{-}in$.. 17

Figure 2.5: The relationship between electrostatic force and spring force vs. gap distance as a function of DC bias voltage when $Vdc=Vpull\text{-}in$.. 18

Figure 2.6: COMSOL 3D model of: (a) A single CMUT cell coupled to a fluid medium, (b) Enlarged image of the 3D CMUT cell, and (c) Simplified cross-section of the CMUT cell model.. 21

Figure 2.7: First five Eigen frequencies (mode shapes) of the designed CMUT membrane and meshed structure: (a) 5.47 MHz, (b) 11.26 MHz, (c) 18.49 MHz, (d) 21.08 MHz, (e) 26.91MHz, (f) Meshed structure... 23

Figure 2.8: Frequency response corresponding to the maximum membrane deflection: (a) in-air, (b) in-immersion........ 24

Figure 2.9: Simulated membrane displacement vs. DC bias voltage, showing the pull-in phenomenon........ 25

Figure 2.10: Analytical and FEA bias voltage vs. static deflection of a single CMUT.......... 26

Figure 3.1: General surface micromachining process for CMUT fabrication [7]........ 28

Figure 3.2: Process flow of CMUT fabrication........ 31

Figure 3.3: Profile measurement result of SiO_2 layer in Wafer map mode........ 32

Figure 3.4: Fabricated CMUT element with a microscopic image for its cells........ 32

Figure 3.5: SEM images of a cross section of a circular CMUT element: (a) Enlarged image of the CMUT cell, (b) Measurement of cavity width of the CMUT cell, (c) Measurements of cavity depth and membrane thickness of the CMUT cell, (d) Miniaturized image of the CMUT cell........ 33

Figure 3.6: The photolithography and etching processes used during the CMUT fabrication........ 35

Figure 4.1: Vibrometer test set-up for air-coupled CMUT........ 36

Figure 4.2: Experimental result of FFT under 35 Vdc and 5 Vac........ 37

Figure 4.3: Transient response of the membrane deflection under 35 V step signal........ 39

Figure 4.4: Corresponding displacement to 35 V step signal in the pull-in curve........ 39

Figure 4.5: Steady state response of the membrane deflection under 35 Vdc and 5 Vac signals........ 40

Figure 4.6: Analytical result of FFT under 35 Vdc and 5 Vac........ 41

Figure 4.7: Analytical and experimental results of FFT of the CMUT........ 42

Figure 4.8: Hydrophone measurement results of the ultrasound signals transmitted by the PZT in both time and frequency domain.. 44

Figure 4.9: Hydrophone measurement results of the ultrasound signals transmitted by the CMUT in both time and frequency domain... 45

Figure 4.10: Measurement results of the ultrasound signals transmitted by the CMUT and received by PZT probe in both time and frequency domain.. 47

Figure 4.11: Measurement results of the ultrasound signals transmitted by the PZT probe and received by CMUT in both time and frequency domain... 48

Figure 4.12: The typical set-up of the in-immersion pulse-echo test..................................... 50

Figure 4.13: Result of the CMUT pulse-echo test of the aluminum block............................. 51

Figure 4.14: Result of the CMUT pulse-echo test of: (a) wall surfaces and 1st hole, (b) wall surfaces and 2nd hole, and (c) wall surfaces and 3rd hole.. 52

Figure 5.1: Illustration of flexible CMUT fabrication process [57]....................................... 56

List of Tables

Table 1.1: Comparison between CMUT and PZT ultrasound transducers...............................2

Table 2.1: Material properties of <100> Si and SiO_2...11

Table 2.2: The parameters of the designed CMUT structure and surrounding medium..........11

Table 4.1: Comparison between the center frequencies of the analytical model, FEA and the experiment...46

Table 4.2: Compared results obtained from the transmission and reception tests of PZT and CMUT...49

List of Abbreviations

MEMS	Microelectromechanical System
NDT	Non-Destructive Testing
CMUT	Capacitve Micromachined Ultrasound Transducer
PZT	Piezoelectric Transducer
SNR	Sound-to-Noize Ratio
A-Mode	Amplitue Mode
AC	Actuating Current
DC	Direct Current
FEA	Finite Element Analysis
3D	Three Dimensions
Si	Silicon
SiO_2	Silicon Dioxide
MHz	Megahertz
KHz	Kilohertz
MRayl	Mega Rayleigh
FFT	Fast Fourier Transform
Si_3N_4	Silicon Nitride
LPCVD	Low Pressure Chemical Vapor Deposition
KOH	Potassium Hydroxide
SOI	Silicon-on-Insulator
RIE	Reactive Ion Etching
DRIE	Deep Reactive Ion Etching

TMAH	Tetramethylammonium Hydroxide
BHF	Buffered Hydrofluoric Acid
PAN	Phosphoric-Acetic-Nitric Acid
DI	Deionized Water
μm	Micrometer
nm	Nanometer
SEM	Scanning Electron Microscope
UV	Ultraviolet
HMDS	Hexamethyldisilazane
dB	Decible
PCB	Printed Circuit Board
FBW	Fractional Bandwidth
FSE	Front Surface Echo
BSE	Back Surface Echo

List of Nomenclatures

c	Speed of Sound
λ	Wavelength
f	Frequency
Z	Acoustic Impedance
R	Sound Reflection Coefficient
Tr	Sound Transmission Coefficient
ρ	Density of The Medium
T	Thickness of The Tested Material
t	Time of Flight of Ultrasound
b_{eq}	Damping Coefficient
k_{eq}	Spring Coefficient
w	Plate Displacement
a	Membrane Radius
t_m	Membrane Thickness
w_{pk}	Membrane Peak Displacement
d_o	Gap Height
t_i	Insulation Layer Thickness
F_{es}	Electrostatic Force
D_o	Flexural Rigidity of The Circular Membrane
E	Young's Modulus,
ν	Poisson's Ratio
C	Capacitance

Q	Charge
ϵ_o	Vacuum Permittivity
A	Area of The Circular Membrane
U	Potential Energy
$V_{pull-in}$	Pull-in Voltage
V_{ac}	AC Voltage
V_{dc}	DC Voltage
m_{eq}	Membrane Equivalent Mass
m_m	Mass of The Membrane
ρ_m	Density of The Membrane
ω_n	Angular Resonance Frequency
f_n	Resonance Frequency
Q_f	Quality Factor
Q_{f_medium}	Quality Factor of The Surrounding Medium
$V_{p\text{-}p}$	Peak-Peak Voltage

Chapter 1

Introduction

1.1 Motivation

Long before the technology for building very small devices were discovered, their potentials were appreciated. Microelectromechanical system (MEMS) has emerged to play a key role in humans' lives, and change their way of living. Ultrasound is one prime method that belongs to MEMS community, which has been employed in a broad scale of applications for numerous aspects of human life. It is, for example, used in industrial NDT, cleaning, diagnosis and therapy in the field of medicine. As technologies advances, different approaches to use ultrasound were proposed. MEMS-based acoustic transducers, suitable for transmitting and detecting ultrasound waves, have been widely researched on ultrasound field. The medical imaging and therapeutic ultrasound dominates high potential for growth in ultrasound applications [18].

Capacitive micromachined ultrasound transducer (CMUT) is one of the recent ultrasound technologies that has branched from MEMS research aspects including modelling [1][2], fabrication [3], [4], and applications [5], [13], [14], [15], [16], by which coveyed numerous interests from both academia and industry. In particular, over the last three decades [6], CMUTs for medical imaging applications have been the foremost interest research groups. However, CMUTs have been proven to be a viable substitute to PZT transducers in terms of NDT applications due to of their straightforward fabrication techniques, large bandwidth [23],[25], small size, improved signal-to-noise ratio (SNR) [26], and compatibility in integrating with an electronic circuits [24]. The fabrication techniques of CMUTs can be

used to implement high frequency and high-density phased arrays leading to higher resolution and higher receive sensitivity ultrasound transducers that can benefit NDT applications [53]. Moreover, the combination of CMUT transducers with the electronic circuit allows one to achieve a highly integrated ultrasound transducer system [53], [54].

Another key characteristic of the CMUTs is that when they are operated in a liquid medium, the vibration of the membrane is damped by the liquid medium; and hence, wider fractional bandwidth, leading to a shorter acoustic pulse and thus a better axial resolution is achieved [12]. The acoustic impedance of CMUTs characteristically matches to the surrounding medium, so matching layers are not required [46]. A comparison between CMUT and PZT transducers is illustrated in Table 1.1.

Table 1.1: Comparison between CMUT and PZT ultrasound transducers.

	CMUT	**PZT transducer**
Fabrication method	Wafer-bonding technology	Ceramic technology
Array fabrication	Difficult	Easy
Fabrication complexity	Easy to fabricate	Hard to fabricate
Fabrication cost	Low cost	High Cost
Characteristic Impedance	Low	High
Frequency Bandwidth	Wide	Moderate
Thermal stability	High	Low
IC integration	Yes	No
Output pressure	Relatively low	High

In spite of CMUTs' outstanding features, there are apparently still limitations to the CMUT technology, such as relatively low output pressure and dielectric charging. The issue of CMUT's low output pressure is due to the limited effective membrane and small gap erea, limiting ultrasound depth of penetration [7], [36], [37]. Higher output pressure offers larger depth of penetration and vice-versa. Figure 1.1 indicates the relationship between the penetration depth and the image resolution as a function of operational frequency.

Efforts from most CMUTs researchers have been carried out to optimize and to improve the functionality and performance of the ultrasound transducers in terms of their transduction efficiency, receive sensitivity and output pressure [8], [9], [10], [11]. The motivation of this project is to further investigate the CMUT behaviors dedicated for NDT applications, since few researches have examined the CMUTs in this field.

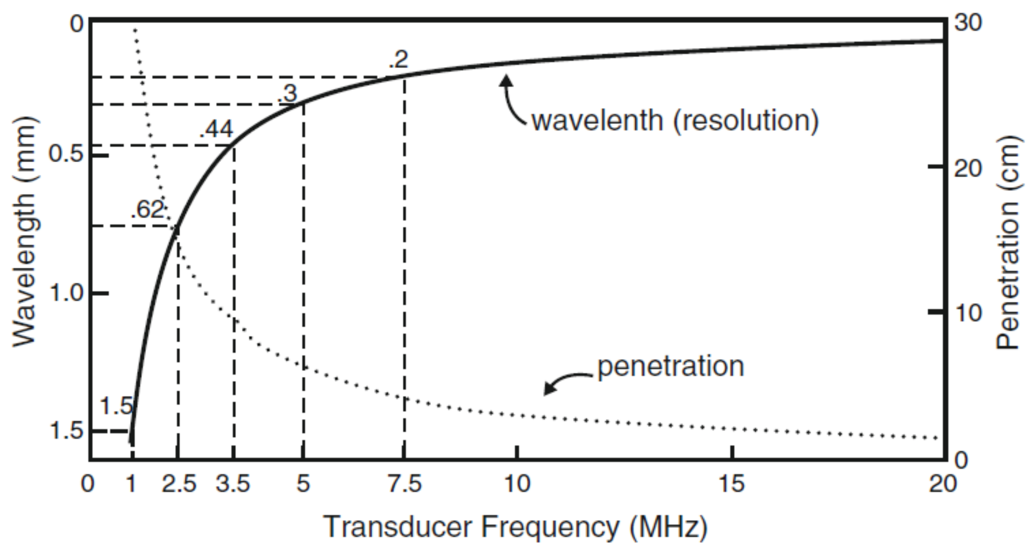

Figure 1.1: Relationship between the penetration depth and the image resolution as a function of operational frequency [42].

1.2 Background on Ultrasound

Ultrasound is basically defined as mechanical waves that propagate within a matter medium due to the particle motion at range of frequencies beyond the average human hearing capacity (>20 KHz). Animals use this acoustic wave for communication and navigation even before it is scientifically established. The typical ultrasound frequency ranges from 1-60 MHz in the diagnostic and therapeutic imaging applications. Ultrasound non-destructive testing (NDT), is one of the ultrasound detection techniques that facilitates inspecting material discontinuities and detects flaws in objects without damaging the tested sample.

Basically, ultrasound NDT testing is performed based on either pulse-echo or through-transmission method. Each of the two types is used in certain applications, but commonly, pulse echo systems are more convenient since they require only one-sided access to the object being inspected as indicated in Figure 1.2. The first ultrasound NDT was proposed in 1929 by Sokolov to inspect concealed discontinuities in metal [17]. Examples of using ultrasound for NDT applications have been investigated using different ultrasound array transducers with different centre frequencies that demonstrate the use of an array to steer the beam through a range of angles to ensure good sensitivity to a range of crack angles in geometrically complex components [29], [30], [31], [55]. Applications in utilizing ultrasound transducers in the aerospace industry to image large areas of uniform geometry have been invistigated as well [32], [33].

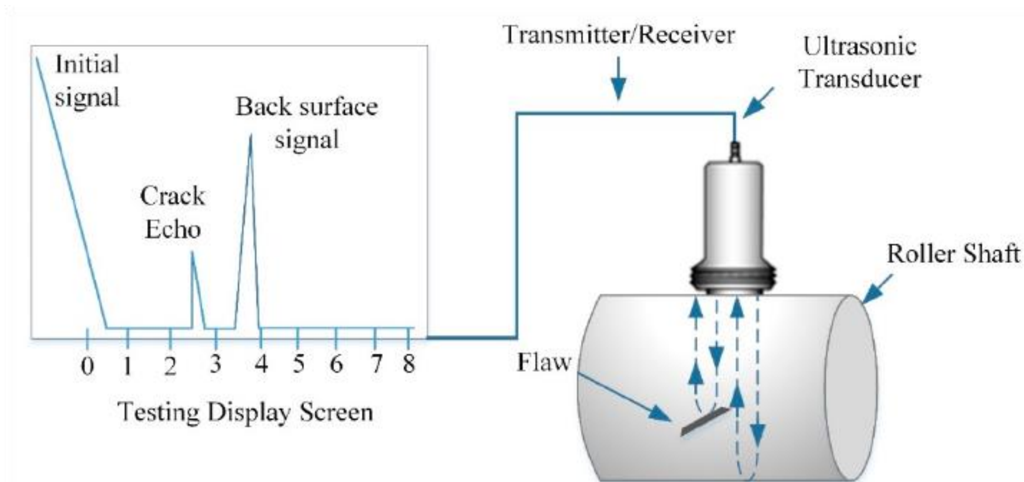

Figure 1.2: A simple pulse-echo test for defined flaw boundary of a material [34].

Ultrasound mechanical waves can come in various forms. The most popular form used in diagnostic and imaging ultrasound is compression, or longitudinal waves. A well-known definition of wave propagation within a matter medium is

$$c = \lambda f \tag{1.1}$$

where c is the speed of sound in a medium, λ is the wavelength, and f is the frequency. With a shorter wavelength, finer features can be spatially distinguished. The inverse relationship between wavelength and frequency means resolution is typically better at shorter wavelengths, and hence at higher frequencies.

Ultrasound signals are reflected at boundaries where there are a difference in the specific acoustic impedance (Z) of the materials on each side of the boundary. The difference in Z is commonly referred to as the impedance mismatch. The greater the impedance mismatch, the greater the percentage of energy that will be reflected at the interface or boundary between one medium and another.

A parameter governing the amount of sound reflected or transmitted at the interface is the Reflection Coefficient [44] and is defined as

$$R = \frac{Z_2 - Z_1}{Z_2 + Z_1} \tag{1.2}$$

where Z_1 and Z_2 are the specific acoustic impedance of the two materials. This means the reflection is stronger when the impedance mismatch is great and vice versa; thus, easier to differentiate between the two layers as depicted in the Figure 1.3. Since the amount of reflected energy plus the transmitted energy must equal the total amount of incident energy, the Transmission Coefficient is calculated by simply subtracting the Reflection Coefficient from one as

$$Tr = 1 - R \tag{1.3}$$

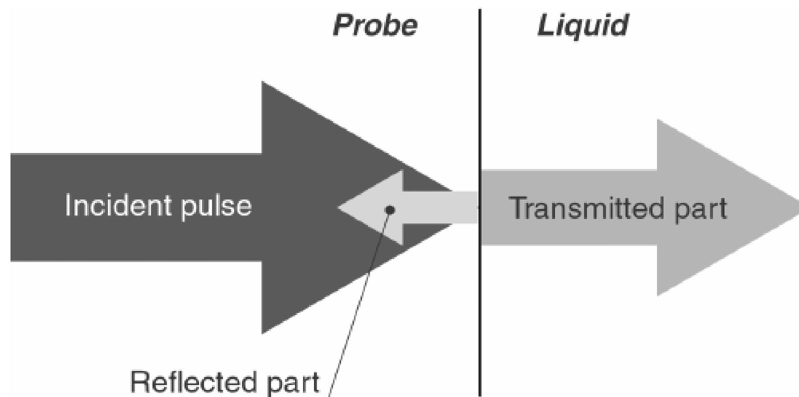

Figure 1.3: Acoustic propagation at the interface of two media.

The specific acoustic impedance of is defined as

$$Z = \rho c \tag{1.4}$$

where ρ is the density of the medium (i.e. steel). In the simplest case of imaging, a 'line of sight', or A-mode, can be acquired after sending an ultrasound pulse and receiving the reflection afterwards, as indicated in Figure 1.2. Two basic quantities are measured in

ultrasound testing; they are time of flight or the amount of time for the sound to travel through the sample, and amplitude of received signal as shown in Figure 1.4.

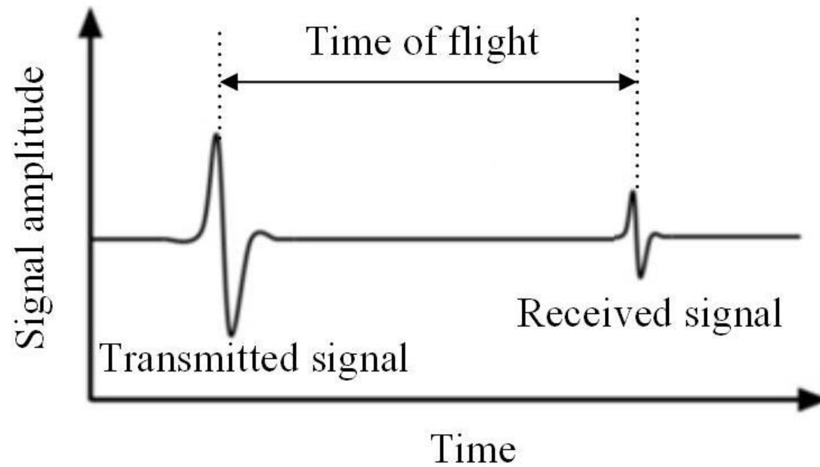

Figure 1.4: A pulse-echo event in the time domain.

Based on velocity and round trip time of flight through the material, the material thickness can be calculated as follows

$$T = \frac{c\,t}{2} \tag{1.5}$$

Where T is the tested material thickness and t is the time of flight of ultrasound.

1.3 Background on CMUT

Conventional ultrasound transducers are made with piezoelectric materials such as lead zirconate titanate (PZT) consisting of a piezoelectric crystal elements, an acoustic matching layer, a backing layer, and an acoustic lens as shown in Figure 1.5. PZT transducers are commonly used in ultrasound imaging due to their high electromechanical conversion efficiency [21]. A typical PZT transducer have an acoustic impedance of approximately 30

MRayl, which is significantly larger than that of air, which is ~400 Rayl [27], leading to narrower operating bandwidths and low signal-to-noise ratio (SNR) [22]. Thus resulting in a significant loss of energy when transferring energy from the transducer to the air. To reduce the impedance mismatch, it requires separate matching and backing layers.

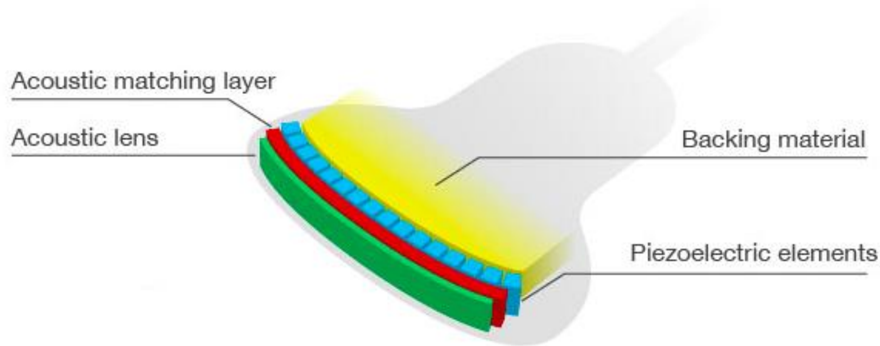

Figure 1.5: PZT Transducer probe structural overview.

Advances in microfabrication technology paved the way to the emergence of CMUTs that were invented by Dr. Khuri-Yakub's research group at Stanford University about eighteen years ago [6]. Since then, they have been considered as a viable alternative technique to PZT transducers due to the outstanding features, stated above. CMUT is principally a parallel plate capacitor commonly utilized for ultrasound applications. A typical CMUT cell configuration is shown in Figure 1.6, which consists of a movable suspended top electrode and a rigid bottom electrode. The top electrode can be the movable membrane itself or resides on it; in this work the top electrode is the conductive membrane of the CMUT. The top and bottom electrodes are isolated from each others by an insulating layer, functionalized in preventing an ohmic contact between the two electrodes and trap electrical charges [19] [20]. A vacuum gap are sealed to boost the device performance and reliability, which allows

the membrane to freely oscillate. An individual CMUT element is made of multiple cells that connected with each other in parallel. A CMUT transducer forms an array when contains multiple elements.

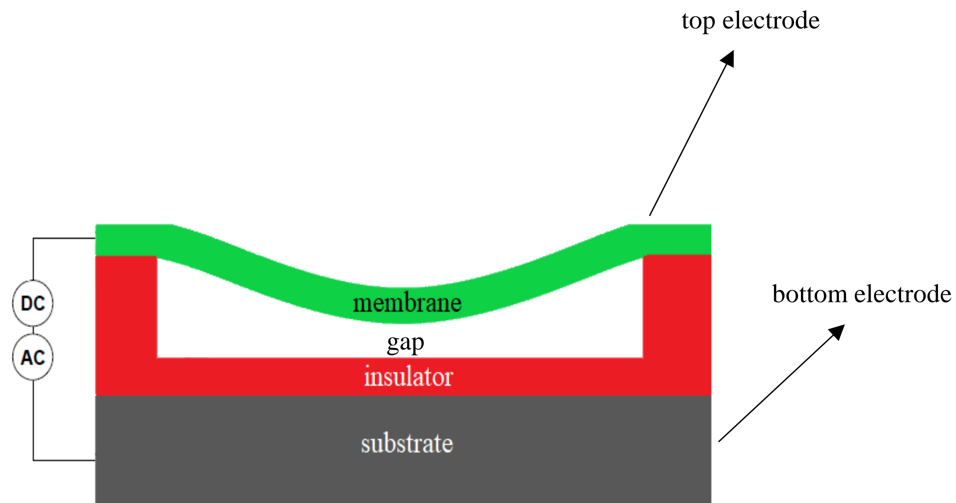

Figure 1.6: Cross-section of a basic unit of a CMUT.

When a DC bias voltage is applied between the bottom electrode and the top electrode, the electrostatic force is generated causing the membrane to deflect toward the substrate. Ultrasound pulses are generated when superimposing an AC voltag on the DC bias voltage causes the membrane to oscillate in an ultrasound frequency range, and thus, the mechanical energy is coupled into the surrounding medium. The dynamic behavior and frequency characteristics of the CMUT are determined by the dimensions and material properties. Under receive mode, the reflected ultrasound waves from the object are detected by the surface of the membrane, inducing a change in the capacitance and produces current that is converted into voltage signals to be measured. Transmit and receive modes of operation can be switched for pulsing and echo detection.

Chapter 2

Modeling of CMUT

Fundamentally, modeling process of the CMUT is critical, by which is considered the prime root of the other related processes. Furthermore, it determines the point to proceeding into the fabrication process. In order to fully comprehend the CMUT's behaviour, *Mathematica*-based mathematical modeling software was initially employed in the first section of this chapter to present the design methodology of the CMUT cells, to develop intuition concerning operation of the device and to extract the fundamental key parameters. The second section of this chapter introduces a 3D finite element Analysis (FEA) simulation, carried out on *COMSOL Multiphysics* to verify the analytical model design. The flow chart below demonstrates the methodology followed to design, simulate and fabricate the CMUTs.

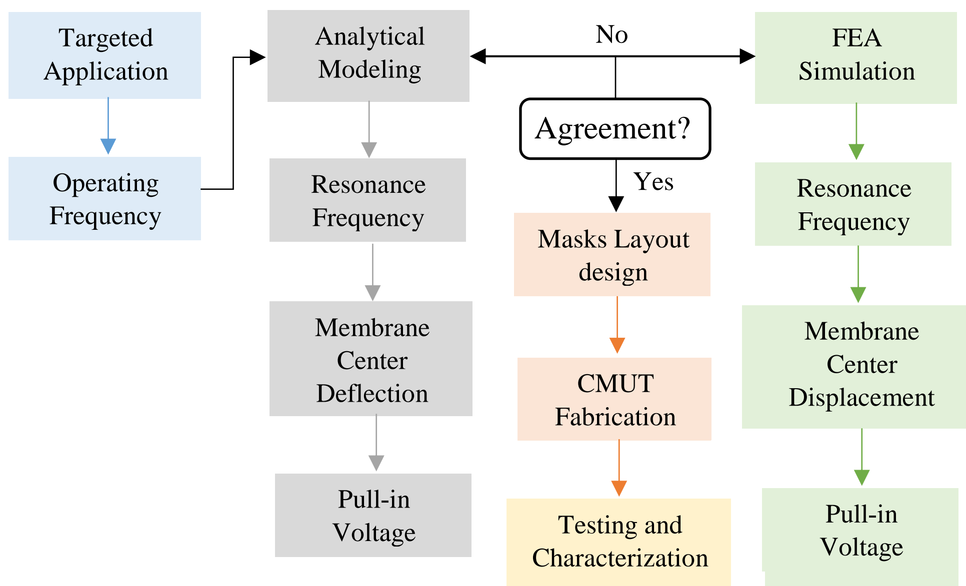

The specific material properties and parameters employed in designing and simulating the CMUT in this chapter are listed in Table 2.1 and Table 2.2, respectively.

Table 2.1: Material properties of <100> Si and SiO_2.

Parameter	**<100> Si**	**SiO_2**
Young's modulus (GPa)	130	70
Poisson's ratio	0.22	0.17
Density (kg/m^3)	2332	2200
Relative permittivity (dielectric constant)	-	3.9

Table 2.2: The parameters of the designed CMUT structure and surrounding medium.

Parameters	**Value**
Membrane radius (μm)	36
Membrane thickness (μm)	2
Insulation layer thickness (nm)	230
Cavity depth (nm)	250
Number of cells	1225
Distance between cells (μm)	12
Speed of sound in air (m/s)	343
Speed of sound in oil (m/s)	1540
Speed of sound in aluminum (m/s)	6320
Density of fluid medium (kg/m^3)	922

2.1 Analytical Modeling

In order to characterize the CMUT's behavior, it is important to model the ultrasound transducer analytically. Analytical modeling would predict the performance of the device at the design stage. Due to complexity of analytical modeling of CMUT, lumped mass model was used [47]. Lumped mass model is a simplified analysis for CMUT, which describes the performance of a spatially distributed system using discrete elements. This method is widely used to approximate the behavior of complex systems by lumping the physical, mechanical, electrical and other properties into discrete elements to reduce the complexity. The accuracy and applicability of the results depend on how realistically the physics of the different components is lumped. A typical system that is converted to the lumped-mass model consists of a point mass, a spring and a damper as shown Figure 2.1.

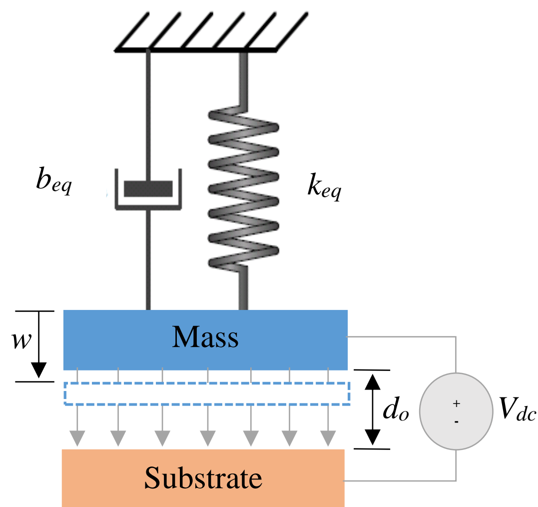

Figure 2.1: CMUT mass-spring-damper system.

The lumped-mass model assumes that the membrane is limited to a small piston-like displacement, i.e., the membrane does not deform. This is practically inaccurate because the membrane deflects more at the center and less towards the clamped edge. Therefore, an accurate adjustment is required to the plate area by applying a shape function based on plate theory [28]. The plate theory is required in order to assure the accuracy of the model. Figure 2.2 displays the CMUT with a deformed membrane and the equivalent circular plate.

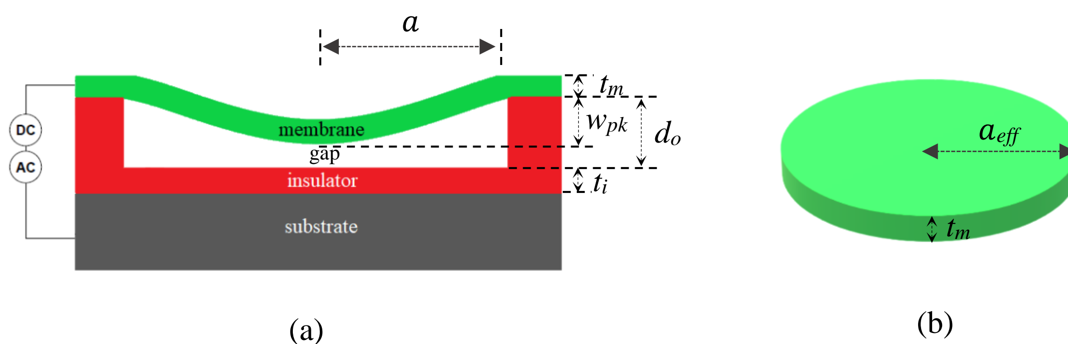

Figure 2.2: (a) Center membrane deflection of a CMUT unit cell, (b) Equivalent plate shape of a circular CMUT membrane.

The CMUT's membrane is designed to be in circular shape due to the fact that the stress of a circular membrane around its edge is least compared to all other membrane shapes [45]. Assuming no external load, the governing equation of motion of the lumped mass system, shown in Figure 2.1 is derived as

$$m_{eq}\ddot{w} + b_{eq}\dot{w} + k_{eq}w = F_{es} \tag{2.1}$$

where w is the displacement of the plate, b_{eq} is the damping coefficient, k_{eq} is the spring coefficient, and F_{es} is the electrostatic force. At the static equilibrium position, the damping and mass forces are vanished, and the spring force, which is also referred to as the mechanical restoring force of the plate, is linearly proportional to the displacement and it is

eventually balanced with the electrostatic force. The linear spring coefficient of the spring force can be written as [48]

$$k_{eq} = \frac{192\,\pi\,D_o}{a^2} \tag{2.2}$$

where a is the membrane radius and D_o is the flexural rigidity of the circular membrane that is described as

$$D_o = \frac{E\,{t_m}^3}{12(1-\nu^2)} \tag{2.3}$$

where E, t_m, and v are the Young's modulus, membrane thickness, and Poisson's ratio of the membrane material, respectively. Assuming the top electrode of the CMUT is displaced by w, the capacitance C of the parallel plate capacitor establishes a linear relationship between charge Q and voltage V across the capacitor plates. The relation is given by

$$\mathrm{Q} = C\mathrm{V} \tag{2.4}$$

The capacitance of the parallel plate capacitor is given by

$$C = \frac{\epsilon_o\,A}{d_o - w} \tag{2.5}$$

where ϵ_o, d_o and A are the vacuum permittivity, gap height and the area of the circular membrane, respectively. The area of the circular membrane is denoted by

$$A = \pi\,a^2 \tag{2.6}$$

Hence, the potential energy in a capacitor is given by

$$U = \frac{1}{2} C V^2 \tag{2.7}$$

The terms of electrostatic force can be derived using Castigliano's Theorem as the negative derivative of the potential energy with respect to the deflection w [58].

$$F_{es} = -\frac{\partial U}{\partial w} = \frac{\epsilon_o A V^2}{2(d_o - w)^2} \tag{2.8}$$

At the equilibrium state, equation (2.1) can be simplified as

$$\frac{\epsilon_o A V^2}{2(d_o - w)^2} - k_{eq} w = 0 \tag{2.9}$$

2.1.1 Pull-in Voltage

The pull-in voltage is one of the critical parameters that needs to be considered when designing CMUTs. Equation (2.9) shows the relationship between the voltage and the plate displacement as

$$V = \sqrt{\frac{2 k_{eq}\, w (d_o - w)^2}{\epsilon_o A}} \tag{2.10}$$

When biasing CMUT with a DC voltage, the membrane deflects towards the bottom electrode due to electrostatic attraction force. The spring force of the membrane balances this deflection. Nonetheless, after a certain limit of increasing the bias voltage, the electrostatic force starts dominating over the spring force and the membrane collapses over the bottom electrode, which known as pull-in voltage. In this case, the pull-in phenomenon typically occurs when the displacement is 1/3 of the gap height ($w_{pull-in} = \frac{1}{3}\, do$). By substituting the calculated displacement into Equation (2.10), the pull-in voltage is obtained as [46]

$$V_{pull-in} = \sqrt{\frac{8 k_{eq} {d_o}^3}{27\, \epsilon_o A}} \tag{2.11}$$

A dielectric material (SiO_2) was used as an insulation layer to avoid the occurrence of short-circuit between the top and bottom electrode. The pull-in voltage of the CMUT membrane was calculated using Equation (2.11), and was obtained at 75 V corresponding to 83 nm displacement as represented in Figure 2.3.

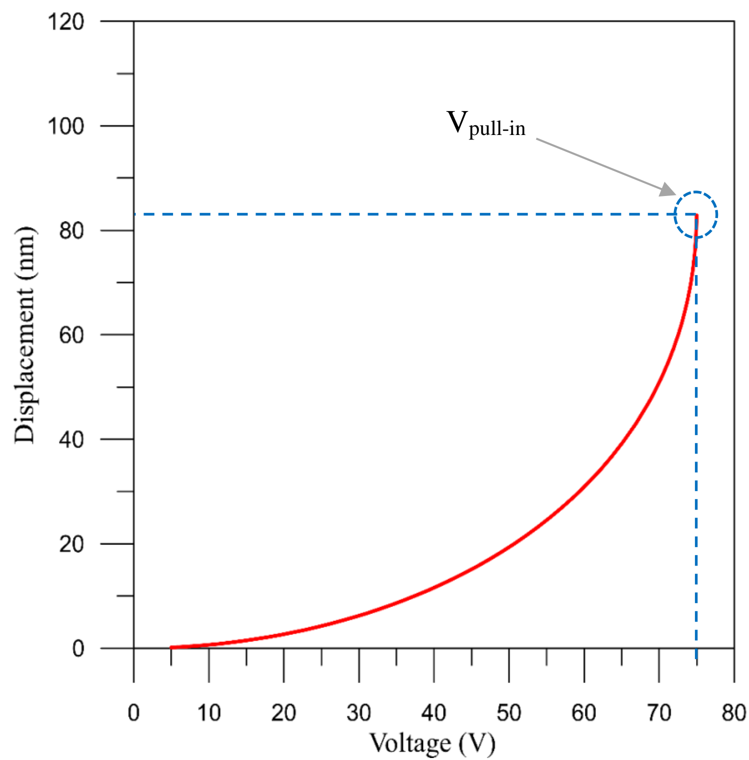

Figure 2.3: Membrane displacement vs. DC bias voltage, showing the pull-in phenomenon.

When increasing DC bias voltage, the gap distance decreases; and hence, the electrostatic force increases. Figure 2.4 and Figure 2.5 show the relationship between electrostatic force and spring force versus gap distance as a function of DC bias voltage. The case when a DC bias voltage is lower than the pull-in voltage is shown in Figure 2.4, which indicates to the membrane equilibrium positions. The stable and unstable equilibrium points appear at the intersection of the two curves. When the membrane is at an equilibrium position

and DC bias voltage is lower than pull-in voltage, the magnitude of electrostatic force and spring force are equal. Thus, two physical solutions are presented.

The first physical solution is indicated as stable equilibrium point, when the stable equilibrium point is disturbed, resulting in increasing the displacement, the spring force becomes greater than the electrostatic force. Therefore, the membrane is pushed back to the stable equilibrium point by the spring force. The second physical solution is indicated as unstable equilibrium point. Instability condition occurs when unstable equilibrium point is disturbed to further increase the displacement and the electrostatic force becomes dominant over the spring force; and hence, the equilibrium is lost.

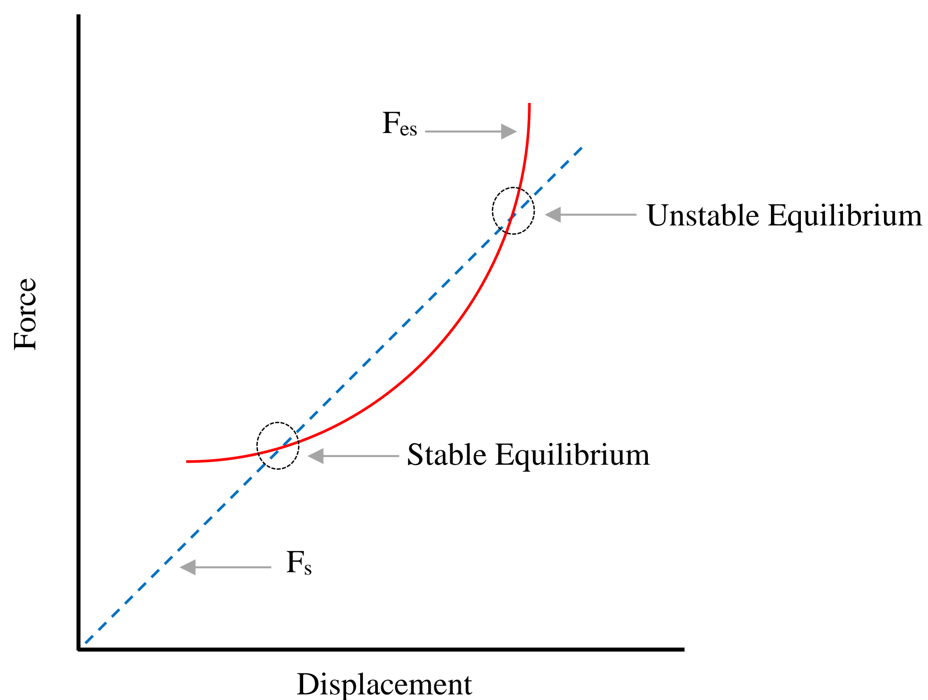

Figure 2.4: The relationship between electrostatic force and spring force vs. gap distance as a function of DC bias voltage when $V_{dc}<V_{pull\text{-}in}$.

As the voltage increases, the electrostatic force increases and eventually the case shown in Figure 2.5 occurs where the spring force line is tangent to the electrostatic force curve. In this case, the stable and unstable equilibrium points meet at the tangent point. This is called the pull-in condition and the corresponding voltage is called the pull-in voltage.

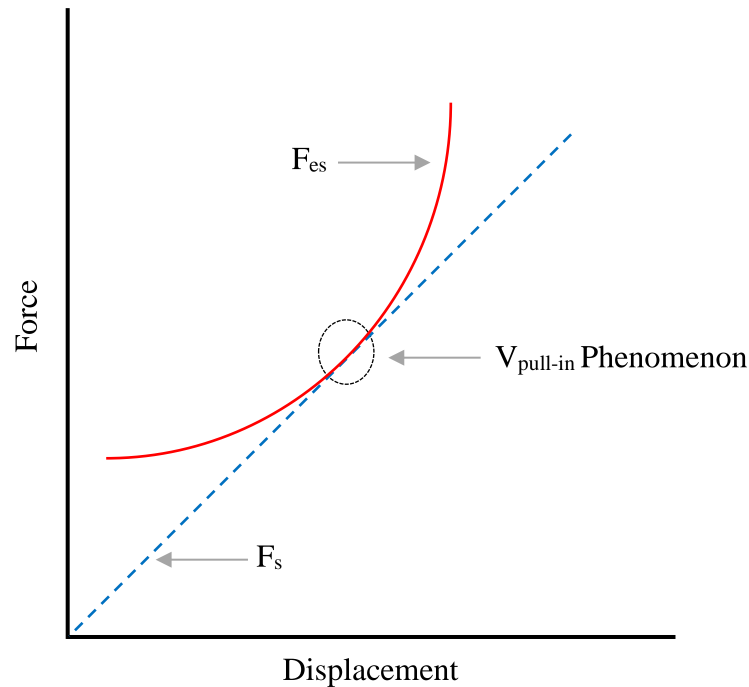

Figure 2.5: The relationship between electrostatic force and spring force vs. gap distance as a function of DC bias voltage when $V_{dc}=V_{pull\text{-}in}$.

2.1.2 Resonance Frequency

Resonance frequency is another key parameter that should be taken into account when designing and modeling CMUTs. A range of frequencies between 0.5 MHz to 2.25 MHz is commonly used in NDT applications as they provide greater energy and penetration in the material, while high frequency transducers (15.0 MHz - 25.0 MHz) provide less penetration but greater sensitivity to locate small discontinuities. Based on the target application, the

resonance frequency of the modeled CMUT is required to be within the range of 2 to 5 MHz. This range of frequency comes from considering penetration depth, material dimensions and type of material to be tested. Thus, The angular resonance frequency of the CMUT can be derived from the lumped mass model as

$$\omega_n = \sqrt{\frac{k_{eq}}{m_{eq}}} \tag{2.12}$$

where m_{eq} is the membrane equivalent mass that can be given as [48]

$$m_{eq} = 1.84\, m_m = 1.84(\rho_m\, A\, t_m) \tag{2.13}$$

where m_m and ρ_m are the mass and density of the membrane, respectively. By substituting Equations (2.2) and (2.13) into Equation (2.12), we get

$$\omega_n = \frac{2.95\, t_m}{a^2} \sqrt{\frac{E}{\rho_m\, (1 - \nu^2)}} \tag{2.14}$$

Hence, the resonance frequency in air for the circular membrane is obtained as

$$f_n = \frac{\omega_n}{2\pi} = \frac{0.47\, t_m}{a^2} \sqrt{\frac{E}{\rho_m\, (1 - \nu^2)}} \tag{2.15}$$

It is obvious that the membrane resonance frequency is proportional to the membrane thickness and inversely proportional to the square of the membrane radius. Based on Equation (2.15) and the parameters listed in the Table 2.1 and Table 2.2, the center resonance frequency in air was calculated at 5.51 MHz.

When operating CMUT in immersion, the damping of the membrane is dominated by the radiation impedance, lowering the membrane resonance frequency [49]; thus, considering the density of the fluid medium, the resonance frequency of the membrane in immersion is obtained by [50]

$$f_n = \frac{\frac{0.47\, t_m}{a^2}\sqrt{\frac{E}{\rho_m\,(1-\nu^2)}}}{\sqrt{1+0.67\frac{\rho\, a}{\rho_m\, t_m}}} \tag{2.16}$$

where ρ is the density of the fluid medium. Based on this equation and the parameters listed in the Table 2.1 and Table 2.2, the center resonance frequency in fluid medium (vegetable oil) was calculated to be 2.26 MHz.

2.2 Finite Element Analysis

Numerical based solutions such as finite element analysis are considered the most widely used methods tool for designing and analyzing MEMS devices. FEA can give an accurate estimation of design, optimization and performance evaluation of MEMs transducers. Researchers have employed FEA to accurately model CMUT devices, based on parallel plate capacitor and piston radiator [43]. In this section, FEA software (*COMSOL Multiphysics*) was used to simulate the CMUT to verify the analytical model design. Accordingly, a 3D model was developed as depicted in Figure 2.6.

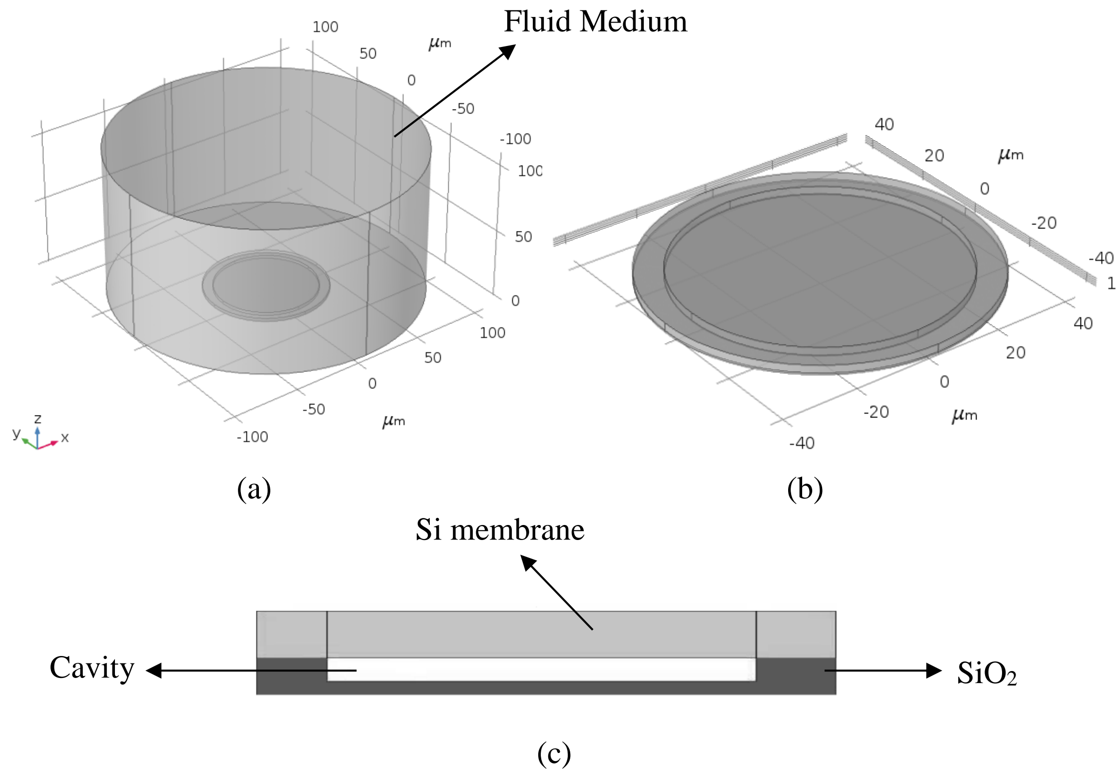

Figure 2.6: COMSOL 3D model of: (a) A single CMUT cell coupled to a fluid medium, (b) Enlarged image of the 3D CMUT cell, and (c) Simplified cross-section of the CMUT cell model.

2.2.1 CMUT Model Set-up

The 3D FEA model consists of a bottom insulation layer, a vacuum cavity, a membrane, and a cylindrical fluid domain. The dimensions and material properties of the membrane, and insulation layer are illustrated in the Table 2.1 and Table 2.2. The cavity material was set to air with relative permittivity of 1, and fluid domain set to vegetable oil.

Electromechanics was applied to the solid domains and the cavity (CMUT structure), under which Linear Dielectric was assigned to the solid domains enabling structural mechanics calculation. Fixed constraint was applied to all solid domains with the exception

of the membrane, which allowed the membrane to vibrate freely. The terminal of the top electrode was applied to the bottom surface of the membrane, while the bottom surface of the insulation layer was grounded. Pressure Acoustics, Frequency Domain was applied to the fluid domain. Under Pressure Acoustics, a background pressure field of 1 atm was applied to the fluid domain, Sound Hard Boundary were applied to the boundary between the top surface of the membrane and medium surface, and plane wave radiation was applied to the surrounding surfaces of the medium. Appropriate boundary settings were applied to fully couple Electromechanics and Pressure Acoustics. In the frequency study part, Stationary and Frequency-Domain Perturbation steps were generated to calculate the CMUT's frequency response.

2.2.2 Eigen Frequency Analysis and Frequency Response

In modeling CMUTs, eigen frequencies and mode shapes are of particular interest. Eigen frequencies present the maximum responses of a system and resemble the characteristics of an underdamped system of CMUT. The first mode is considered the fundamental vibration mode that gives the maximum center displacement. The other modes had non-uniform membrane shapes and would therefore generate a non-uniform pressure radiation [51]. Using the parameters, listed in Table 2.1 and Table 2.2, the first five mode shapes and the meshed structure of CMUT were obtained as shown in Figure 2.7.

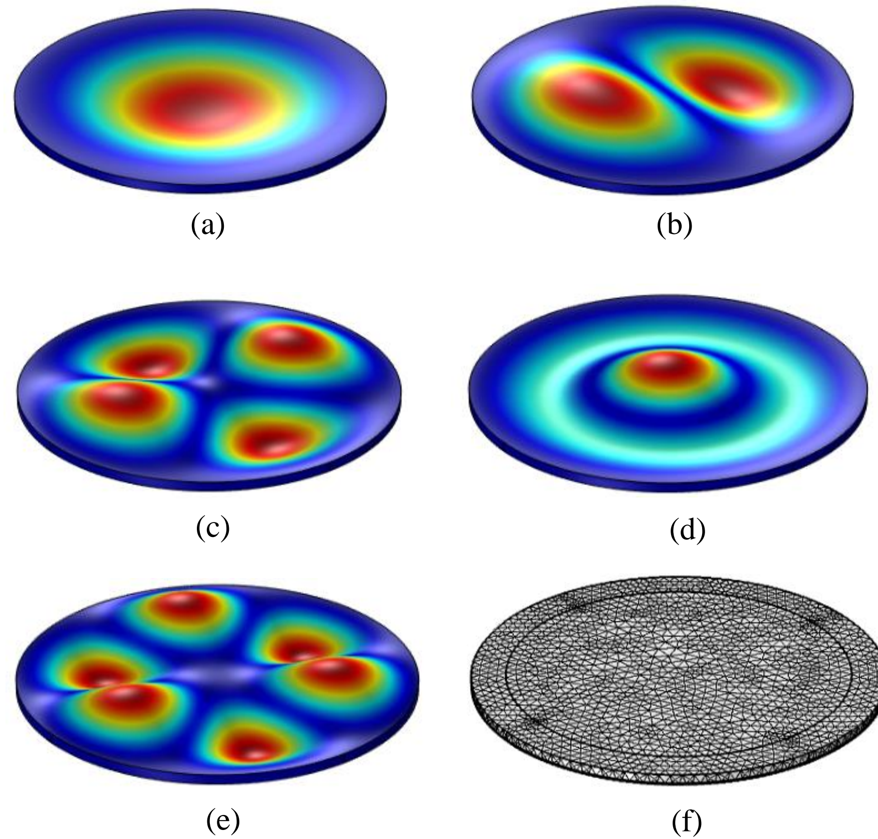

Figure 2.7: First five Eigen frequencies (mode shapes) of the designed CMUT membrane and meshed structure: (a) 5.47 MHz, (b) 11.26 MHz, (c) 18.49 MHz, (d) 21.08 MHz, (e) 26.91MHz, (f) Meshed structure.

The fundamental in-air and in-liquid resonance frequencies corresponding to the maximum membrane deflections were simulated. Stationary and Frequency-Domain Perturbation steps were generated in the frequency study part (frequency sweep) in order to obtain the CMUT frequency responses. As shown in Figure 2.8, when the CMUT given 35 DC bias voltage and 5 AC voltage, the in-air and in-immersion resonance frequencies corresponding to the maximum membrane deflections were obtained as 5.47 MHz and 2.19 MHz, respectively. The responses show a good agreement with the results calculated using the analytical model. It is observed that when operating CMUT in a liquid medium, the liquid

mass loading leads to higher damping that contributes in lowering the resonance frequency [49]; and hence, smaller membrane deflection and wider bandwidth are achieved comparing with that in-air.

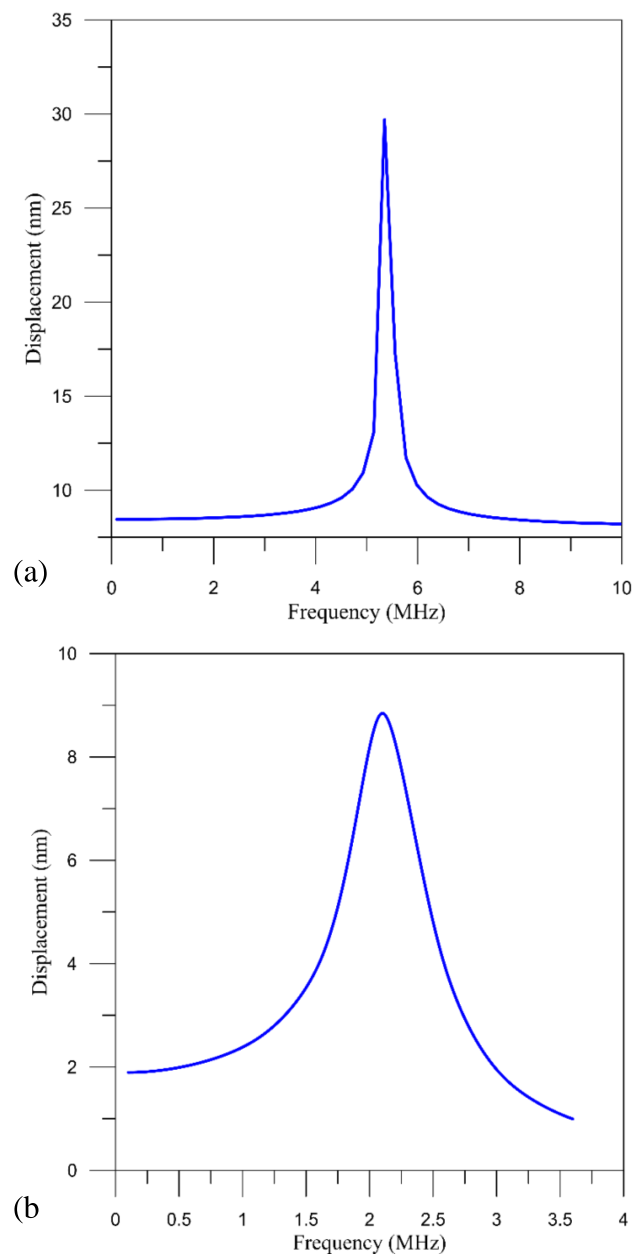

Figure 2.8: Frequency response corresponding to the maximum membrane deflection: (a) in-air, (b) in-immersion.

2.2.3 Pull-in Voltage Phenomenon

A parametric study was performed on the designed CMUT to observe its nonlinear behavior under an applied DC bias voltage and to avoid the membrane instability at the pull-in voltage. Therefore, a range of 0 V to 80 V DC bias voltage was applied on the membrane to observe the membrane deflection as a function of the static bias voltage. When an electrical potential is applied, the membrane undergoes an electric displacement due to the force caused by the applied voltage. The maximum displacement of the membrane occurs at its center. The pull-in voltage was calculated at 74.9 V corresponding to 78.5 nm displacement as depicted in Figure 2.9. A comparison between analytical and FEA models in calculating the pull-in voltage phenomenon is shown in Figure 2.10.

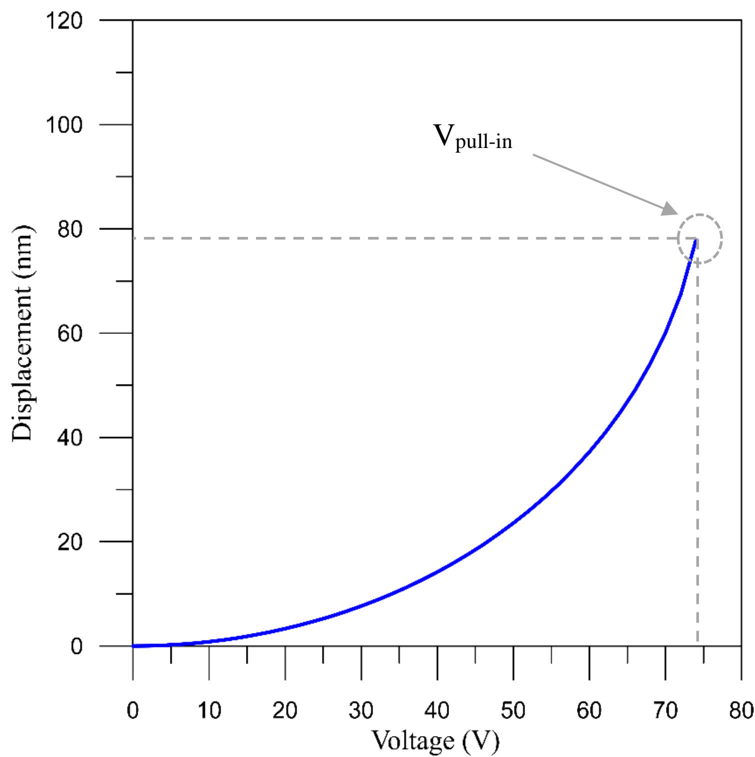

Figure 2.9: Simulated membrane displacement vs. DC bias voltage, showing the pull-in phenomenon.

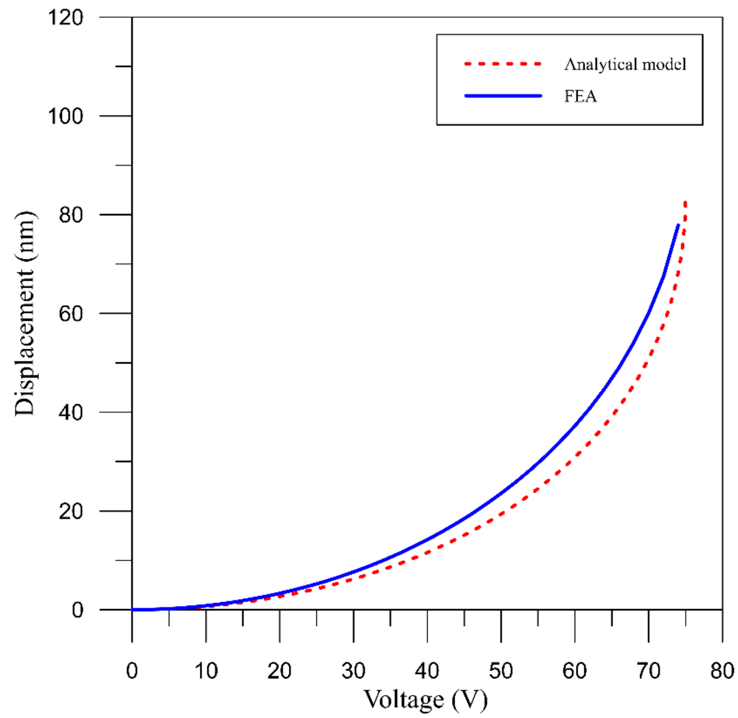

Figure 2.10: Analytical and FEA bias voltage vs. static deflection of a single CMUT.

The difference in the pull-in voltage curves is expected because the FEA is a multi-degree of freedom model and will capture the pull-in voltage more accurately than the single degree of freedom model used in the lumped-mass model. Overall, the results obtained from analytical model and FEA simulation are in good agreement.

Chapter 3

CMUT Fabrication

One of the major advantages of CMUTs is their microfabrication process due to a miniaturized footprint and enhanced performance. The common CMUTs fabrication can be categorized into two processes, by either surface micromachining or the wafer bonding process.

3.1 Surface Micromachining Process

The CMUT fabrication based on surface micromachining method has been widely studied since its origin in 1994 [38], [39], [40]. A typical surface micromachining process is depicted in Figure 3.1. The fundamental factor in fabricating CMUTs using surface micromachining process is to achieve cavity structures that allow membrane to vibrate. In surface micromachining process, depositing and patterning the structure of the CMUT are accomplished layer by layer. In the first step, a low pressure chemical vapor deposition (LPCVD) process is used to deposit a silicon nitride (Si_3N_4) etch-stop layer on a highly doped silicon wafer, acted as a substrate (step b). In the next step, depositing a polysilicon sacrificial layer on the silicon nitride layer by LPCVD process (step c). In the following step, the sacrificial layer is patterned and dry-etched for forming channels that stop at the silicon nitride layer (step d). Another LPCVD process is done to grow a thin sacrificial layer that later defines the thickness of the CMUT cavities (step e). Subsequently, a Si_3N_4 layer is deposited on the sacrificial layer by LPCVD to seal the cavities and to define the membrane (step f). The next step is to etch out holes in the silicon nitride layer by photolithography and dry etching (step g). The holes are etched out from the silicon nitride layer in order to later

reach the sacrificial layer. The step is followed by releasing the membrane and defining the cavities using potassium hydroxide (KOH) wet etching (step h). After that, LPCVD process is performed to grow a thin silicon nitride layer for cavities sealing. Before the final step, the silicon nitride layer is patterned and dry etched to expose the bottom electrodes (step j). Eventually, sputtering, photolithography and wet etch steps are done for the aluminum layer to achieve the top and bottom bonding pads (step k).

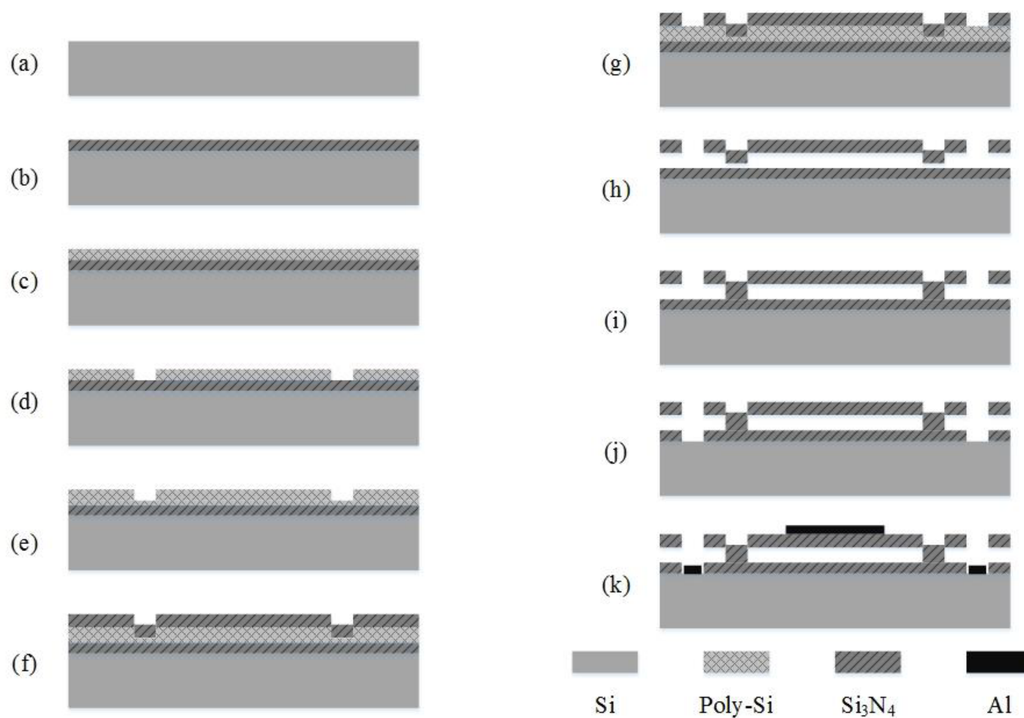

Figure 3.1: General surface micromachining process for CMUT fabrication [7].

3.2 Wafer Bonding Process

Compared to the surface micromachining process for CMUT fabrication, the standard direct wafer bonding process was selected in this research due to the straightforwardness of its processes, unique yield, better uniformity and process control [4]. Furthermore, the most advantage of the wafer bonding technique is the reduction in the number of masks used during the fabrication process, and consequently a lower cost. Additionally, wafer-bonded CMUTs have no etched holes and channels for the membrane release. As a result, a higher sensitivity is achieved due to the increased active area [11].

The process flow to fabricate the CMUT is shown in Figure 3.2 (a-f). Each CMUT cell was designed to have a circular shape with a 36 μm radius membrane. The fabrication initiates with two wafers (top and bottom). The bottom wafer is a 4-inches Boron-doped, single side polished silicon wafer in <100> orientation with a thickness of 500 μm and has a low resistivity of 0.001-0.005 Ω-cm, which allows the bottom wafer to be directly used as the bottom electrode. The top wafer is a silicon-on-insulator (SOI) wafer of which its device layer will serve as the membrane. The device layer is made of 2 μm Boron-doped silicon with orientation of <100> and has a high resistivity of 1-20 Ω-cm. In the first step of the fabrication process, ~ 480 nm oxide film is thermal grown on the bottom silicon wafer in a furnace (Tytan 4600 Mini Fourstack Horizontal Furnace, TYSTAR), as illustrated in Figure 3.2 (a-left). To assure from the oxide layer thickness grown on Silicon wafer, the SiO_2 film profile was measured using profile measurement equepmint (Filmetrics-F50). Thus, a result as shown in Figure 3.3 points out to the measurement of the oxide layer thickness, grown on the silicon substrate. Then as shown in Figure 3.2 (a-left), a photolithography step is done to pattern the cavities and a subsequent dry reactive ion etching (RIE) step is performed by using CF_4 and O_2 gases in the process to etch out the 250 nm deep cavities. Figure 3.2 (a)

indcates to the direct bonding process for the top and bottom wafers. Before the wafers direct bonded, both the SOI wafer and bottom wafer were treated by wet chemical and Oxygen plasma activations. The wafers were first cleaned with RCA-1 and RCA-2 solutions at 80 ˚C for 15 mins for each to attain a contamination-free construct. Thereafter, both wafers were activated with oxygen plasma for 10 min to enhance the surface activity. After RCA-1 and RCA-2 cleanings and oxygen plasma activation, the top and bottom wafers are then direct bonded with the wafer bonding machine (AWB-04 aligner wafer bonder, Applied Microengineering Ltd) with a 2800-kN compressive force for 10 min right after the plasma treatment. Following the pervious process, the bonded wafer then annealed at 1100 ˚C for 4 hours to achieve a permanent covalent bonding.

After the bonding process completed, the bonded wafers are immersed into a buffered hydrofluoric acid (BHF) for several seconds to remove the very thin native oxide layer grown as a result of the direct bonding process; thus, to accelerate the etching rate of the top handling layer of SOI wafer, tetramethylammonium hydroxide (TMAH) solution was used. The top handling layer of SOI wafer, as indicated in Figure 3.2 (b), was removed by 25% of TMAH solution at 80 °C. In this step, the buried oxide layer provided a TMAH etch stop. The buried oxide layer was then removed by the BHF solution that stopped at the device silicon layer as shown in Figure 3.2 (c). Subsequently, the device silicon layer was patterned by the photolithography and a deep reactive ion etching (DRIE) (PlasmaPro Estrelas100, Oxford Instruments plc) step was followed to etch out the device silicon layer, releasing the CMUT membrane as depicted in Figure 3.2 (d). In the next step, as shown in Figure 3.2 (e), a hole for the bottom electrode connection was patterned on the silicon oxide layer by the photolithography process and RIE step was followed in order to expose the bottom silicon substrate for electrode connection. In the last step, an aluminum metal layer with thickness of

~170 nm was sputtered by a metal sputter system, then patterned by the photolithography process. Subsequently, a wet PAN (648 mL Phosphoric acid + 54 mL Acetic acid + 27 mL Nitric acid + 135 mL DI water) etching process was followed to form the top and bottom metal pads of the CMUT, as shown in Figure 3.2 (f). After the fabrication process from Figure 3.2 (a) to Figure 3.2 (f) was completed, dicing the wafer into small chips step was performed on the wafer in order to obtain separate devices. The dicing was done using a dicing saw equipment (Disco Automatic Dicing Saw DAD3240). During the fabrication process, 4 physical masks that were fabricated at the NanoFab Centre at University of Alberta, were employed to entirely fabricate the CMUT device. The fabricated CMUT is shown in Figure 3.4.

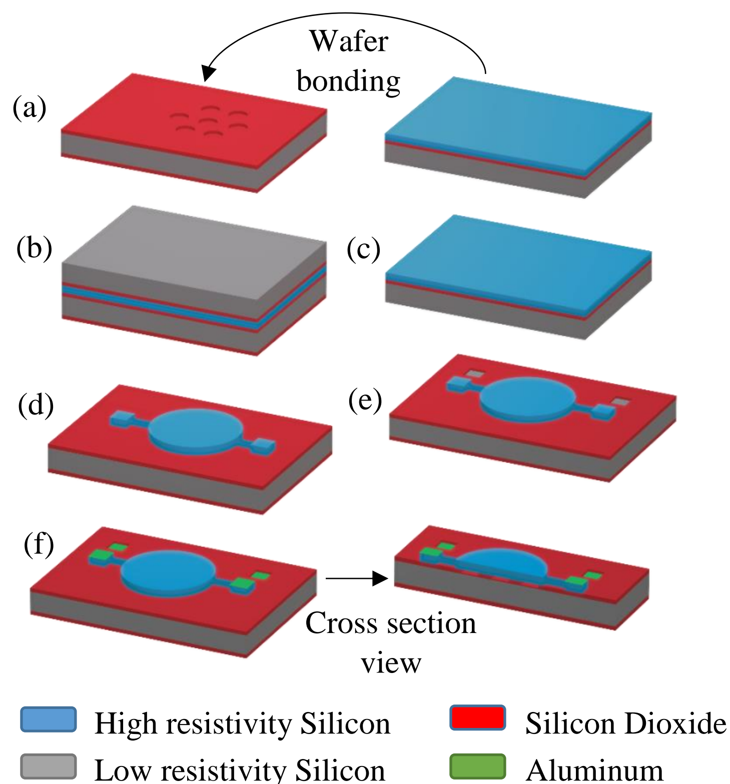

Figure 3.2: Process flow of CMUT fabrication.

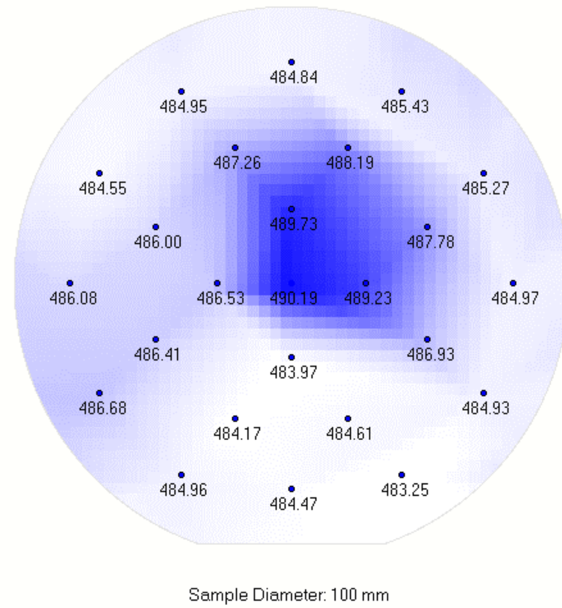

Figure 3.3: Profile measurement result of SiO_2 layer in Wafer map mode.

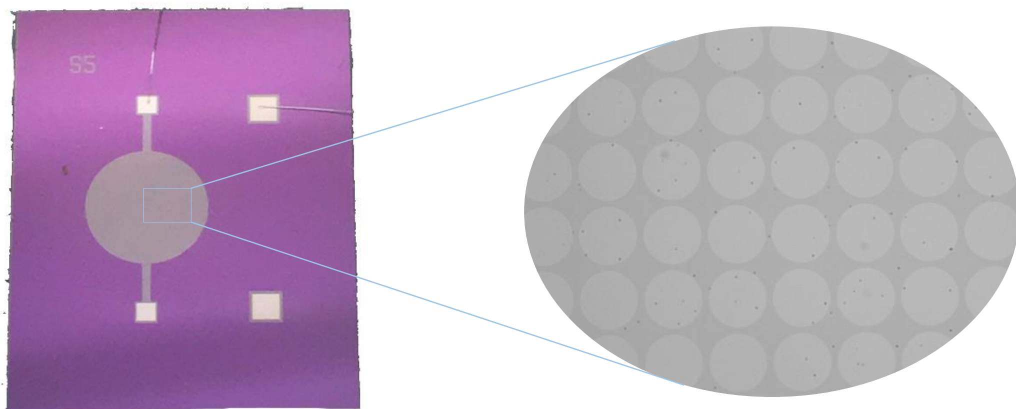

Figure 3.4: Fabricated CMUT element with a microscopic image for its cells.

After obtaining separate CMUT devices, Optical Scanning Electron Microscope (SEM) images of a cross sectional CMUT element, as shown in Figure 3.5, were taken to characterize the CMUT structure and to measure the layers' profile. The diameter of the CMUT element was measured to be 3 mm.

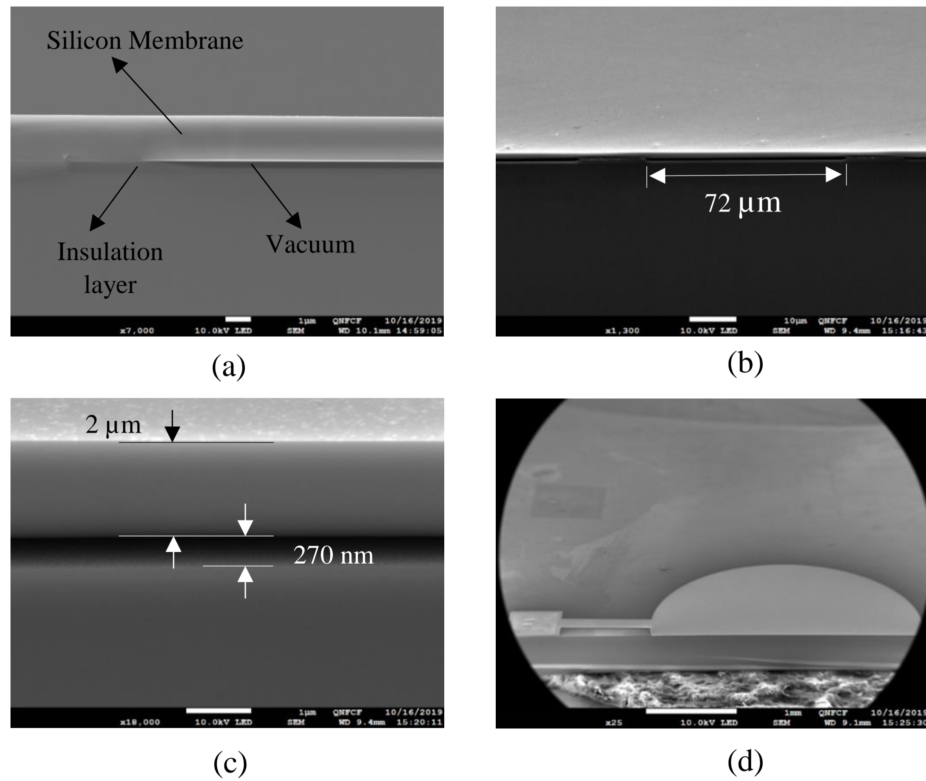

Figure 3.5: SEM images of a cross section of a circular CMUT element: (a) Enlarged image of the CMUT cell, (b) Measurement of cavity width of the CMUT cell, (c) Measurements of cavity depth and membrane thickness of the CMUT cell, (d) Miniaturized image of the CMUT cell.

3.2.1 Photolithography Process

Photolithography is a process used in microfabrication from the stage of transferring geometric shapes on a thin or a thick film wafer until the photoresist removal step. Photolithography relies on a light-sensitive coating, known as a photoresist, which resists etching. A physical mask with geometric shapes is aligned onto the wafer to allow selective exposure of the photoresist to ultraviolet (UV) illumination. After UV exposure, the photoresist is developed with a developer, and the areas of the photoresist exposed to the UV

light are then washed away to be etched normally. The photolithography process, performed in this research started with a spin coating a thin positive photoresist (AZ 3312) on the wafer using specific spin coating recipes based on the wafer and thickness of the photoresist; thereafter, the photoresist was pre-baked at 90 ^{o}C for 2 minutes in a hotplate in order to thermally dry the resist film which would otherwise stick to the photomask. In some cases, the resist film may not work during the next developing process; thus, a thin layer of Hexamethyldisilazane (HMDS) could pre-applied and baked on the wafer as a photoresist adhesion promoter. After pre-baking the photoresist, alignment and exposure steps were performed using Mask aligner (MA6) equipment. A physical mask with a specific patterns was aligned onto the wafer and exposed to UV light. UV light is selectively weakens the exposed photoresist and transfer the pattern from the photomask into the photoresist. Subsequently, the photoresist was developed by a developer solution (AZ 300 MIF). Then, the areas of the photoresist exposed to the UV light were washed away to be etched. Post-baking at 110 ^{o}C for 2 minutes of the photoresist step was followed right after the developing process to stabilize and harden the developed photoresist prior to proceeding to the etching step. The bare exposed areas were then dry or wet etched to reach the desired etching geometry. Eventually, the leftover photoresist was removed away with a stripper solution, ending the photolithography and etching processes. The photolithography and etching processes used during the entire fabrication process are illustrated in the Figure 3.6.

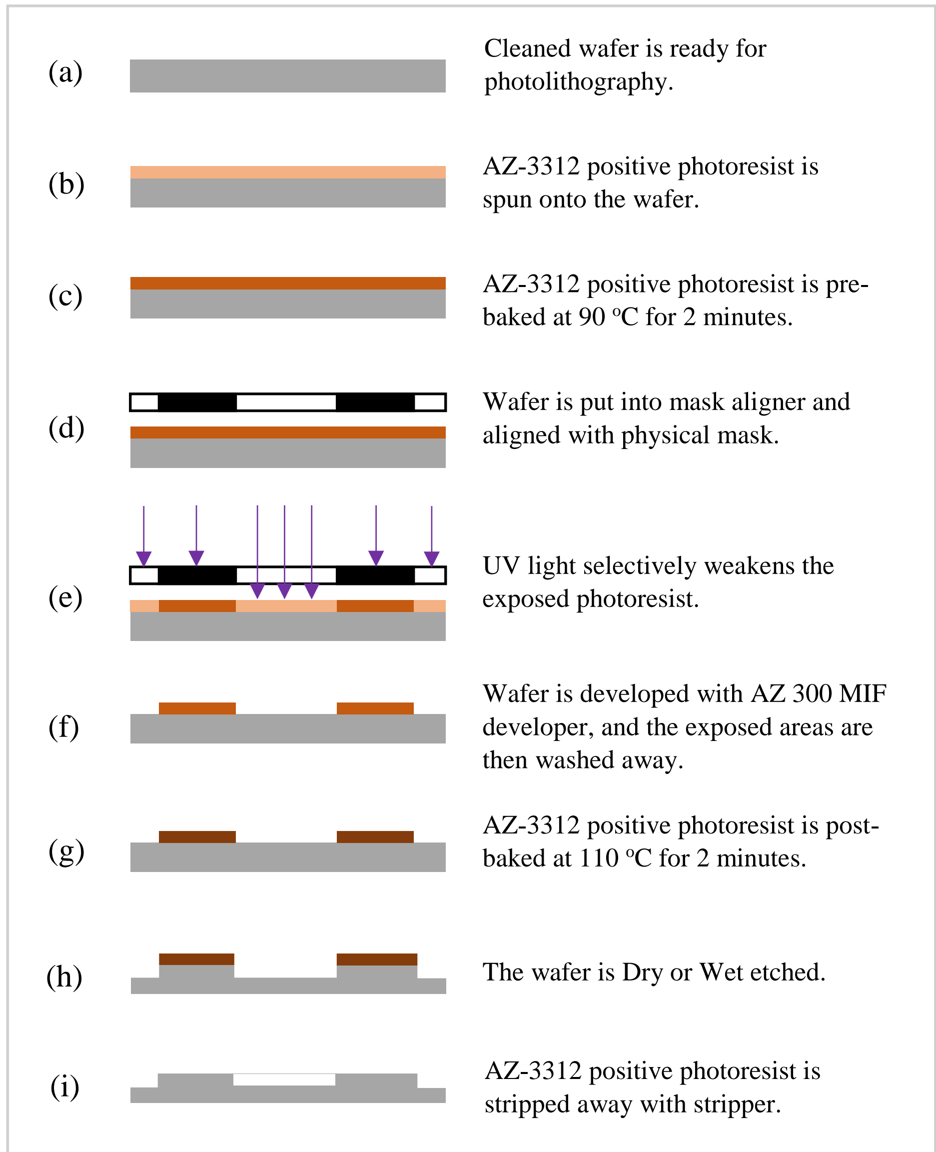

Figure 3.6: The photolithography and etching processes used during the CMUT fabrication.

Chapter 4

CMUT Testing and Characterization

4.1 Air-coupled Characterization

Air-coupled experiment as shown in the Figure 4.1 was carried out on CMUT in order to measure in-air resonance frequency, as well as to characterize the CMUT displacement under bias DC and small AC signals. The experiment was also performed to validate the effectiveness of the results acquired from the modelling analysis.

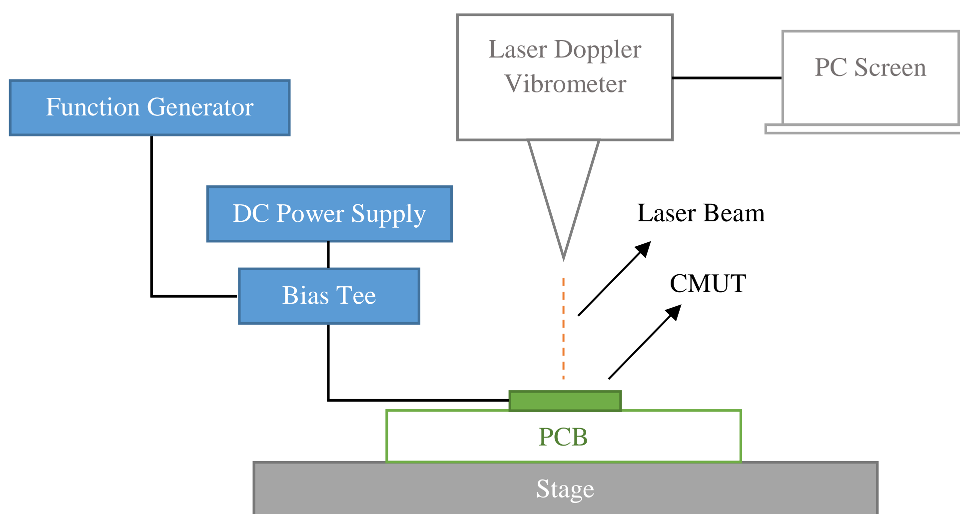

Figure 4.1: Vibrometer test set-up for air-coupled CMUT.

An air-coupled test was carried out on the CMUT using a Laser Doppler Vibrometer (Polytec OFV-5000, DD-300 displacement decoder). The vibrometer was utilized to characterize the in-air resonance frequency and membrane deflection under DC bias voltage and AC sinusoidal signal. The experiment was also conducted in order to validate CMUT

operation. Using a function generator (Tektronix AFG3022B) with a frequency sweep function and feeding the CMUT with a 35 V DC bias voltage along with 5 V_{p-p} AC continuous sinusoidal signal, we observed that, the CMUT resonated at 5.51 MHz with a 15 nm maximum deflection.

After obtaining the CMUT resonance frequency, the CMUT was excited with 35 V DC bias voltage and 5 V_{p-p} AC at a frequency of 5.51 MHz to calculate the FFT of the CMUT. The result of FFT, obtained experimentally is shown in Figure 4.2.

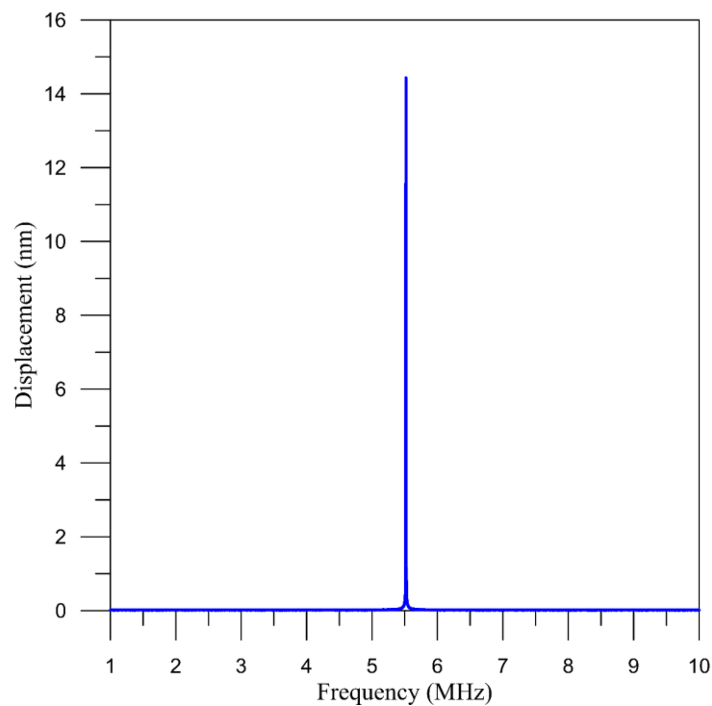

Figure 4.2: Experimental result of FFT under 35 V_{dc} and 5 V_{ac}.

4.1.1 Dynamic Analysis

In order to perform a dynamic analysis of CMUT, the value of quality factor (Q_f) should be firstly obtained. The quality factor (Q_f) of a resonator is commonly defined as the ratio of the maximum energy stored to the energy dissipated per cycle by damping processes. For a vacuum-sealed CMUT cell, the medium damping is the dominant loss mechanism [52]; therefore, $Q_f = Q_{f_medium}$. Since the system is underdamped, which exhibits an oscillatory behavior, the value of quality factor was initially extracted from the frequency response, obtained experimentally to be $Q_f = 16$. The obtained value of the Q_f was then employed in the analytical approach to verify the experimental result of FFT. The quality factor value functions in the damping part of the equation, by which a high quality factor corresponds to low damping and vice versa.

The transient response of the CMUT was initially investigated under a DC step signal. Dividing the Equation (2.1) by the equivalent mass m_{eq} and using a DC step signal, we obtain

$$\ddot{w}(t) + \frac{\omega_n}{Q}\dot{w}(t) + \omega_n w(t) = \frac{\epsilon_o A {V_{dc}}^2}{2 m_{eq} (d_o - w(t))^2} \tag{4.1}$$

Using the Equation (4.1), the CMUT cell was initially biased with 35 V step signal and the transient response of the membrane was tracked for 5 μs as represented in Figure 4.3. It is noticed that the oscillation dies out at 8.564 nm, which is the same value that corresponds to the 35 V in the pull-in curve, as shown in Figure 4.4.

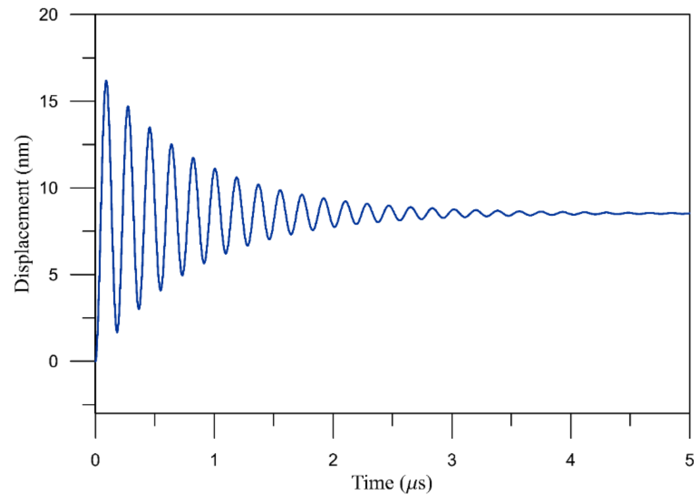

Figure 4.3: Transient response of the membrane deflection under 35 V step signal.

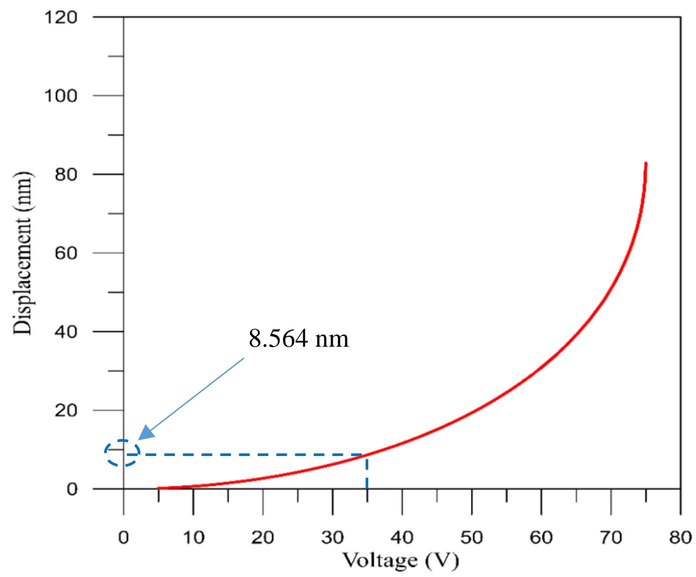

Figure 4.4: Corresponding displacement to 35 V step signal in the pull-in curve.

After obtaining the CMUT transient response, the steady state response of CMUT under DC and AC signals was obtained by using Equation (4.2)

$$V = V_{dc} + V_{ac}\, sin(2\pi f t) \tag{4.2}$$

where f is the frequency of the excitation in (Hz). Substituting this voltage in the Equation (4.1), we obtain

$$\ddot{w}(t) + \frac{\omega_n}{Q}\dot{w}(t) + \omega_n w(t) = \frac{\epsilon_o\, A\,(V_{dc} + V_{ac}\, sin(2\pi f t))^2}{2\, m_{eq}\,(d_o - w(t))^2} \tag{4.3}$$

The CMUT was given a 35 V_{dc} bias voltage and 5 $V_{p\text{-}p}$ AC voltage at 5.51 MHz frequency of the excitation, the steady state response of the membrane was tracked for 5 μs and the AC peak to peak displacement was found to be around 17 nm, when excited at 5.51 MHz as shown in Figure 4.5.

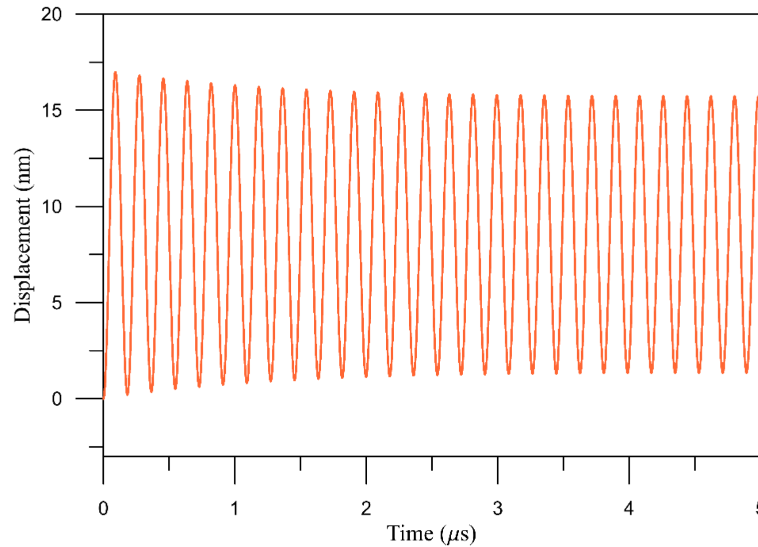

Figure 4.5: Steady state response of the membrane deflection under 35 V_{dc} and 5 V_{ac} signals.

The analytical result of FFT of the CMUT, as shown in Figure 4.6, was then obtained from the steady state response, indicated above.

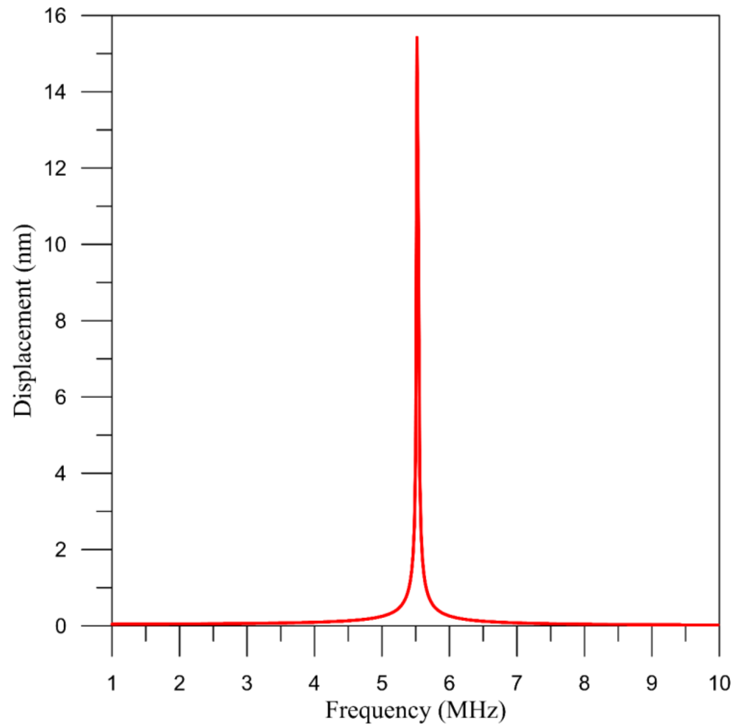

Figure 4.6: Analytical result of FFT under 35 V_{dc} and 5 V_{ac}.

In order to validate the value of quality factor, the FFT obtained analytically in Figure 4.6 was compared with the FFT result, obtained by the vibrometer test, shown in Figure 4.2. When comparing the experimental result with that obtained from the analytical model, as shown in Figure 4.7, it is noted that the peak of FFT obtained analytically is slightly higher than the one obtained experimentally. Overall, the results from the both approaches are in close agreement.

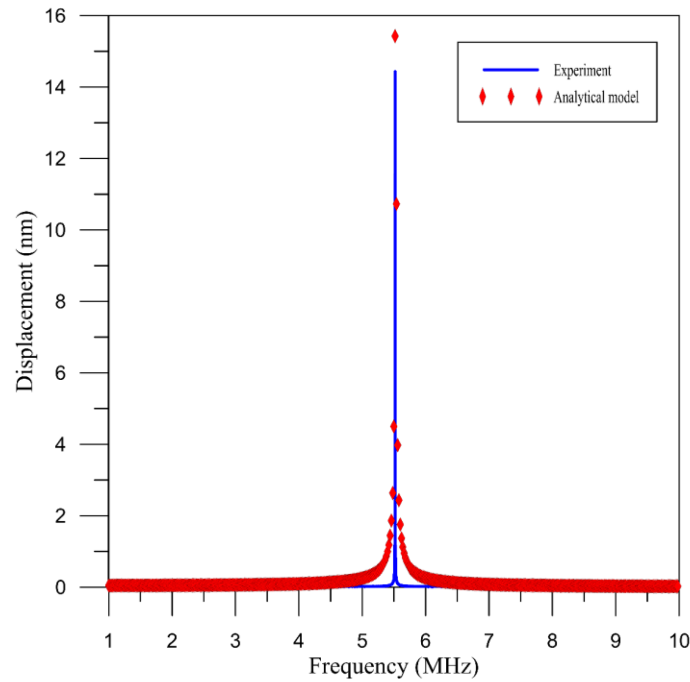

Figure 4.7: Analytical and experimental results of FFT of the CMUT.

4.2 In-immersion Testing and Characterization

In-immersion characterization of CMUT was conducted in liquid medium in order to maintain a consistent coupling between the CMUT transducer and tested sample with easily controlling the CMUT while testing [35]. In this research, the vegetable oil was used as liquid medium due to it acts as an insulator medium that precludes a short circuit between the electrodes of the CMUT. The main purpose of performing in-immersion experiments is to acquire some of key characteristics for the CMUT including output pressure, receive sensitivity, center frequency and fractional bandwidth. The output pressure determines the penetration depth; receive sensitivity locates small discontinuities; center frequency is determined by the application; the fractional bandwidth determines the resolution of the system. Furthermore, in-immersion pulse-echo test was conducted on a flawed aluminum reflector in order to examine the real flaws.

4.2.1 PZT and CMUT Transmission Tests

The first test of in-immersion experiments was conducted to characterize the transmission performance of CMUT and Olympus piezoelectric transducers (PZT) in terms of their output pressure and frequency bandwidth. The absolute value of the total output pressure and frequency bandwidth of the received signals can be measured with a needle type hydrophone. A Fourier Transform is performed on the received signals to determine the frequency bandwidth. A pulser/receiver (Panametrics NDT 5073PR) was employed to drive the PZT probe, and a hydrophone (Onda HGL-0200) was used to catch the PZT acoustic signal. The hydrophone was placed 19 mm away from the PZT transducer and connected to a digital oscilloscope (Agilent DSO7104B) through a pre-amplifier (Onda AH-2010). To achieve a maximum receiving signal amplitude, the hydrophone was aligned to the center of the PZT transducer by adjusting its position while keeping it 19 mm away from the transducer. Figure 4.8 shows the received signal captured by the hydrophone in both time and frequency domains. Based on the frequency spectrum, the center frequency and -6 dB fractional bandwidth (FBW) of PZT were 2.29 MHz and 45%, respectively; close to that provided by the manufacturer (2.24 MHz center frequency and 43% FBW). Based on the sensitivity of the hydrophone-pre-amplifier combination, provided by the manufacturer (0.322 mV/kPa), the output pressure of the PZT was calculated to be 279.5 kPa based on the maximum peak-to-peak output voltage (90 $mV_{p\text{-}p}$).

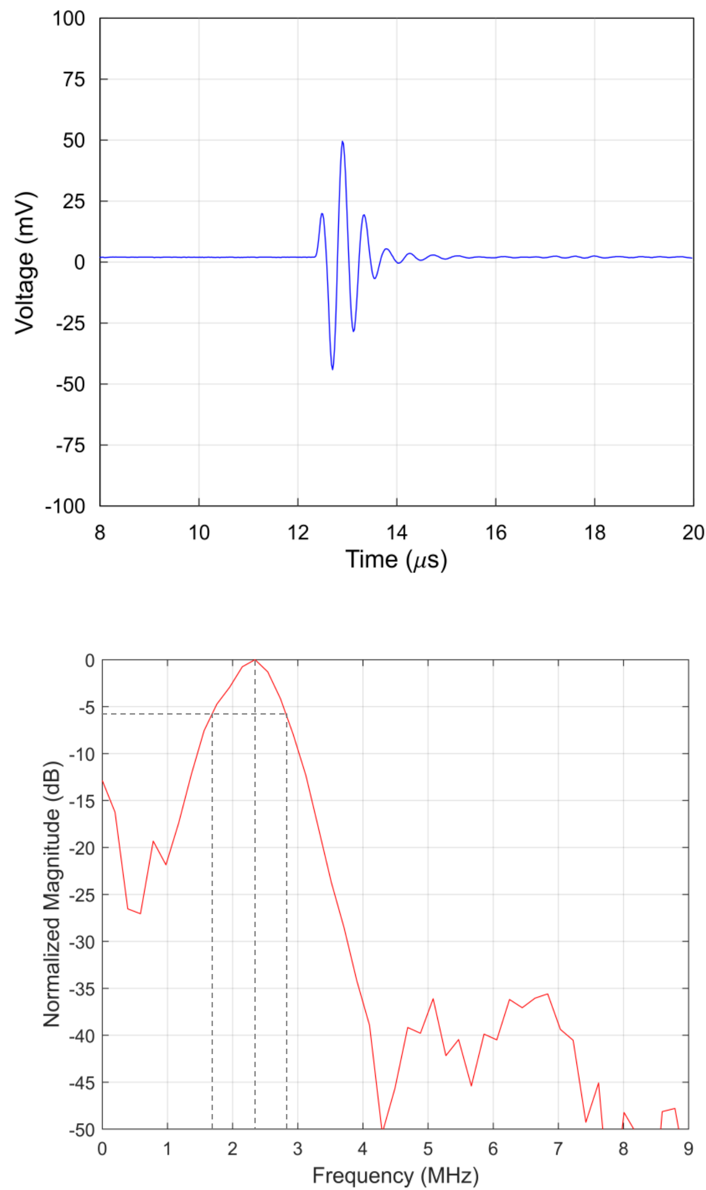

Figure 4.8: Hydrophone measurement results of the ultrasound signals transmitted by the PZT in both time and frequency domain.

The same test was also performed on the CMUT to examine the transmission performance in terms of the output pressure and frequency bandwidth. Biasing the CMUT with 20 V DC, the received signal captured by the hydrophone in both time and frequency domains are shown in Figure 4.9. The resulted center frequency and -6 dB fractional bandwidth

were obtained as 2.22 MHz and 189%. Accordingly, the output pressure of the CMUT was calculated at 62.11 kPa based on the maximum peak-to-peak output voltage (20 $mV_{p\text{-}p}$).

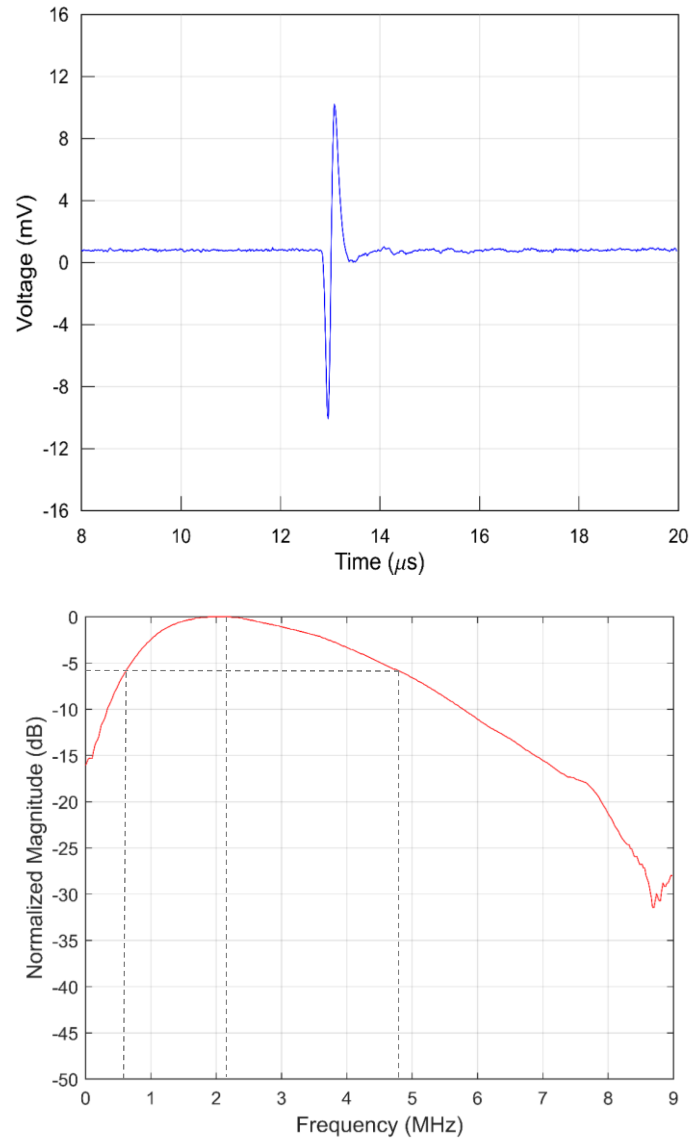

Figure 4.9: Hydrophone measurement results of the ultrasound signals transmitted by the CMUT in both time and frequency domain.

To verify the validity of the analytical model and FEA results in terms of the in-air and in-immersion CMUT center frequency, Table 4.1 compares their results with experimental measurements. Therefore, the three approaches are in close agreement.

Table 4.1: Comparison between the center frequencies of the analytical model, FEA and the experiment.

Parameter	Analytical model	FEA	Experiment
in-air center frequency (MHz)	5.51	5.47	5.51
in-immersion center frequency (MHz)	2.26	2.19	2.22

4.2.2 PZT and CMUT Reception Tests

The reception tests were conducted for both PZT and CMUT to characterize their receive sensitivity. Receive sensitivity of the PZT probe and CMUT can be evaluated by the ratio of the received sound signal to the corresponding acoustic pressure. The PZT probe was characterized first, which was acted as a receiver to detect the signals propagated from the CMUT element. The PZT probe was driven by the pulser/receiver (Panametrics NDT 5073PR) that was then connected to the digital oscilloscope (Agilent DSO7104B), functioned in presenting the received signals. The transmitter-CMUT was placed 21 mm away from the PZT probe and was biased at 20 V DC. The ultrasound signal detected by the PZT probe is shown in Figure 4.10. The maximum peak-to-peak output voltage of the received signal was determined to be 300 $mV_{p\text{-}p}$; accordingly, the translated receive sensitivity was calculated at 4.83 mV/kPa.

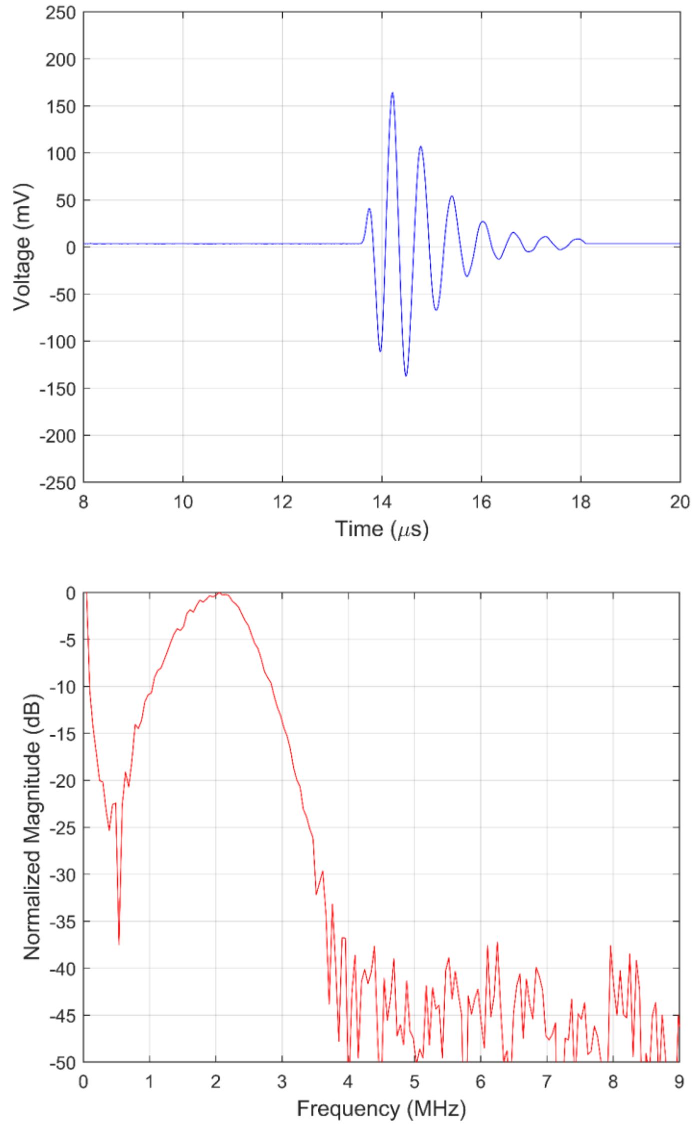

Figure 4.10: Measurement results of the ultrasound signals transmitted by the CMUT and received by PZT probe in both time and frequency domain.

Subsequently, the receive sensitivity test of the same CMUT, used in transmission test was characterized. The receiver-CMUT was wire bonded to a printed circuit board (PCB) with a transimpedance amplifier with a gain of 20 kΩ. The transimpedance amplifier was used to amplify and convert the signal from the CMUT to voltage signals. The receiver-CMUT was placed 21 mm away from the transmitter PZT probe and was biased at 20 V DC.

The captured signal is presented in Figure 4.11. The maximum peak-to-peak output voltage of the amplifier was measured as 1.935 V. Accordingly, the receive sensitivity of the CMUT-transimpedance amplifier combination was calculated to be 31.15 mV/kPa.

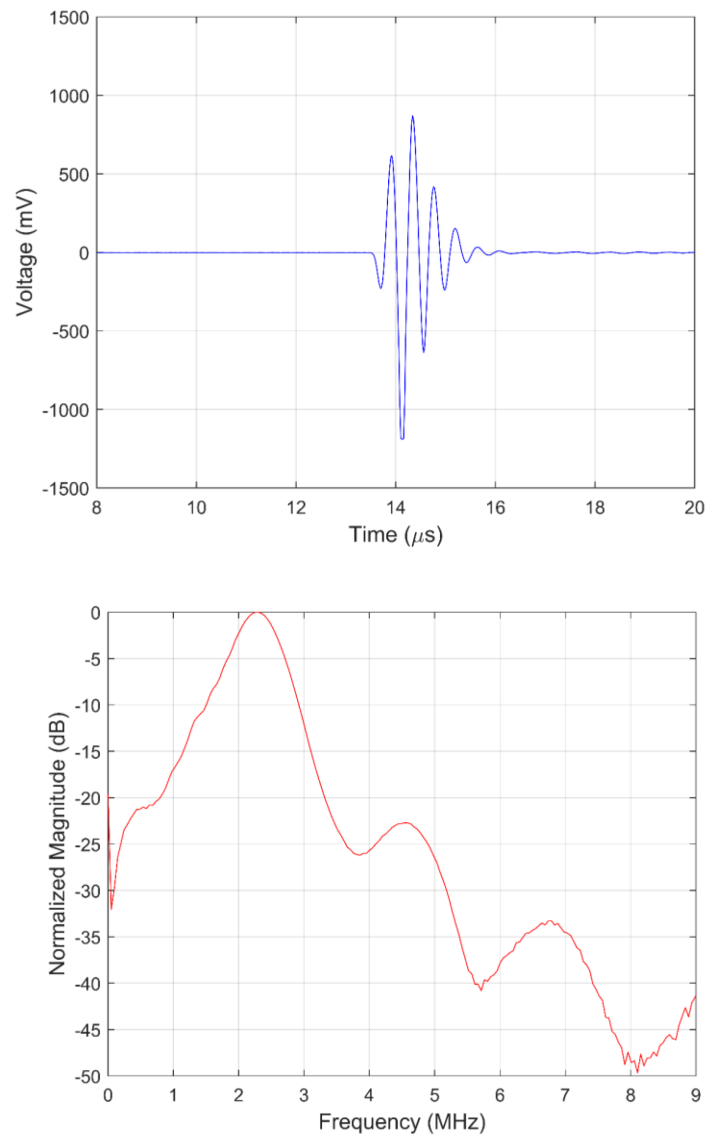

Figure 4.11: Measurement results of the ultrasound signals transmitted by the PZT probe and received by CMUT in both time and frequency domain.

Comparison between the results obtained from the transmission and reception tests of the PZT probe and the CMUT are presented in Table 4.2. Compared to the PZT transducer, the CMUT has approximately four times of the bandwidth and half the output pressure. It can also be observed that the -6 dB frequency range of the CMUT completely covers that of the PZT probe. The frequency spectrum of the two transducers were excellently matched as designed.

Table 4.2: Compared results obtained from the transmission and reception tests of PZT and CMUT.

Parameter	PZT probe	CMUT
Center frequency (MHz)	2.29	2.22
-6 dB bandwidth	45%	189%
Output pressure (kPa)	279.5	62.11
Receive sensitivity (mV/kPa)	4.83	31.15

4.2.3 CMUT Pulse-echo Tests

A typical set-up of the in-immersion pulse-echo ultrasound test, conducted in this research, is shown in Figure 4.12. The set-up consists of several functional units, including the pulser/receiver (Panametrics NDT 5073PR), CMUT transducer (2 MHz), and a display oscilloscope device (Agilent DSO7104B). The pulser/receiver is utilized to generate high voltage electrical pulses. The CMUT is driven by the pulser to generate high frequency ultrasound energy that is presented and propagates through the tested sample in the form of waves. When there is a flaw (such as a crack) in the wave track, part of the energy will be reflected back from the flaw surface, and then transformed into an electrical signal by the CMUT's transimpedance amplifier, and is displayed on a screen. Given the speed of sound, the round-trip can be directly related to the distance that the sound wave traveled. Thus, information about the material location, size, and orientation can be gained.

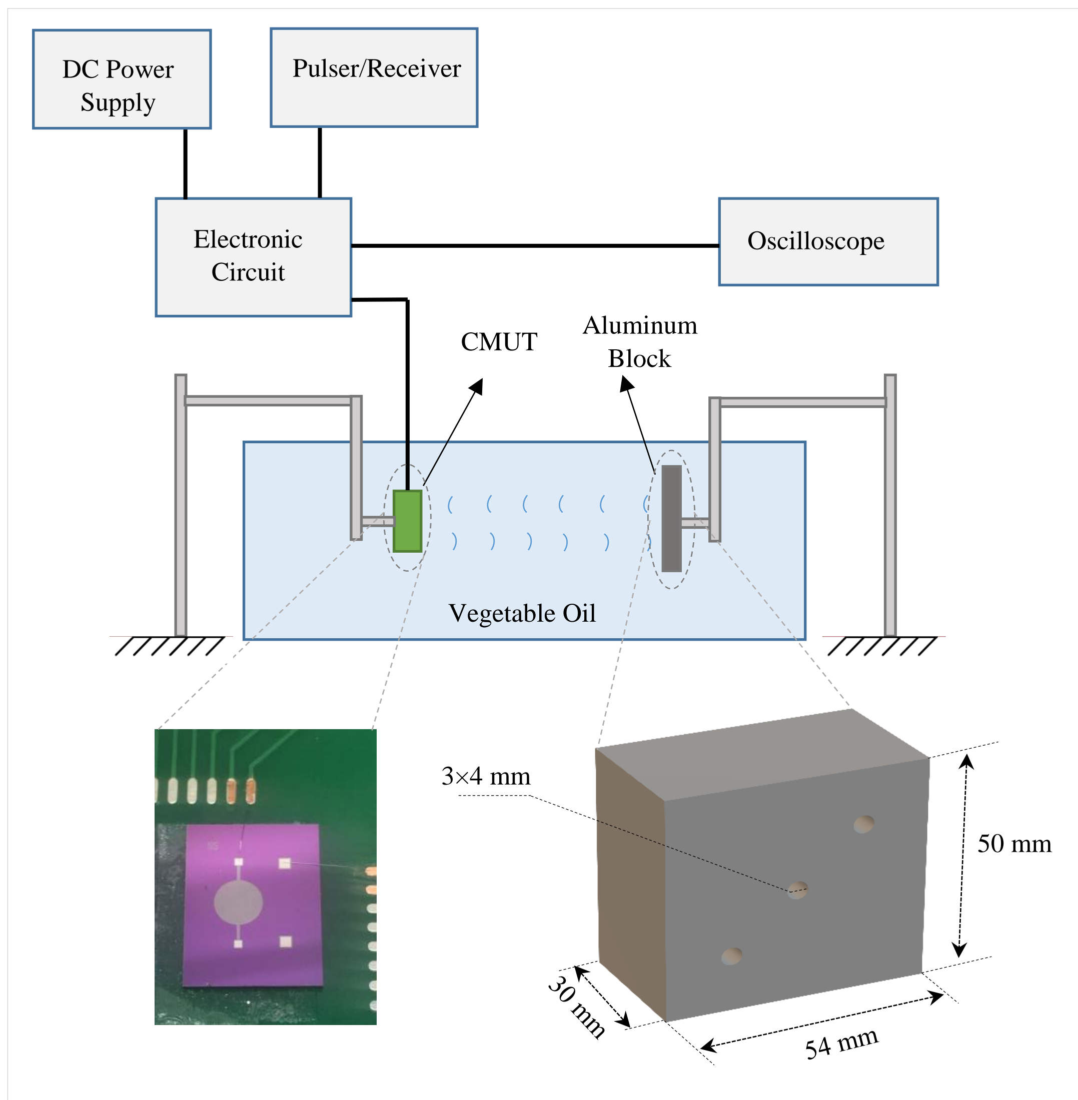

Figure 4.12: The typical set-up of the in-immersion pulse-echo test.

The first pulse-echo test was conducted on an intact 50 mm-thick aluminum reflector (no flaws) that was placed 30 mm away from the CMUT transducer. The wire-bonded CMUT-PCB was connected to an external electronic circuit, linked to the pulser/receiver device. The CMUT was biased at 20 V DC and driven by the pulser/receiver, providing ultrasound pulses. The signal, reflected from the aluminum block was then transformed to an

electrical signal and amplified by the transimpedance amplifier to be displayed in the oscilloscope device. Figure 4.13 depicts the signal reflected from the aluminum block and received by the CMUT. Based on the speed of sound of the medium and reflector, 1540 m/s and 6320 m/s, respectively, the round-trip of the ultrasound wave was calculated. Thus, the front surface (FS) and back surface (BS) echoes of the aluminum block were distinguished. From the Figure 4.9, FSE and 1st BSE represent the front surface echo and first back surface echo, respectively. The 2nd BSE and 3rd BSE represent the second and third back surface echoes, reflected within the test block. Two successive back surface echoes represent a round trip in the block.

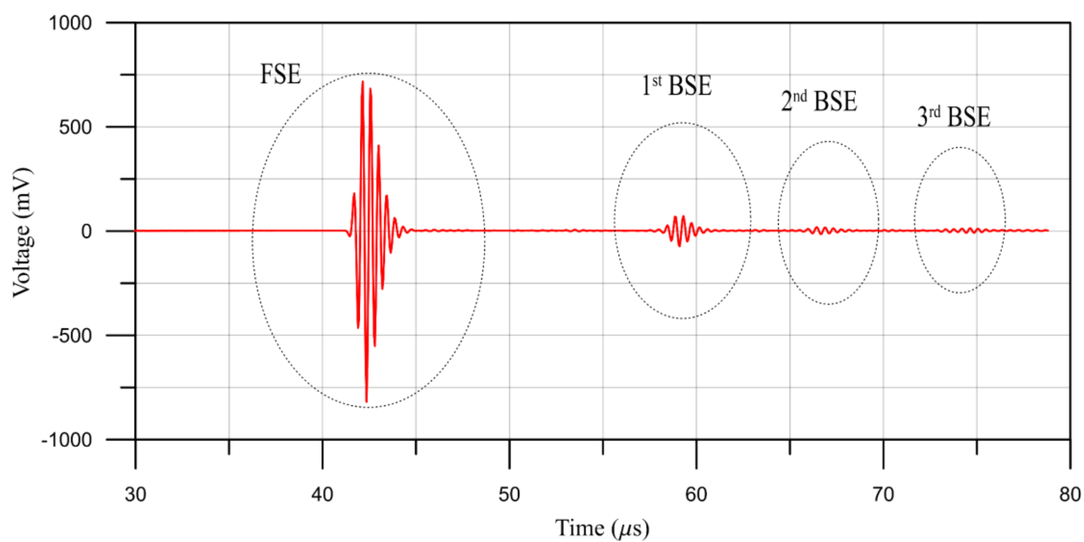

Figure 4.13: Result of the CMUT pulse-echo test of the aluminum block.

Three holes (flaws-like) were then made in the aluminum reflector to be tested and characterized with the CMUT pulse-echo test. The distance of the three holes from the front surface of the aluminum block are 12.5, 25 and 37.5 mm, respectively. The same round-trip test set-up used in the first pulse-echo test was applied to the flawed reflector. The pulser connected to the 20 V DC biased CMUT, generating ultrasound pulses. The signals, reflected from the flaws and external surfaces of the aluminum block were then transformed to

electrical signals and amplified by the transimpedance amplifier to be demonstrated in the oscilloscope device. Figure 4.14 represents the signals reflected from the three holes, and front and back surfaces of the aluminum block, which were received by the CMUT.

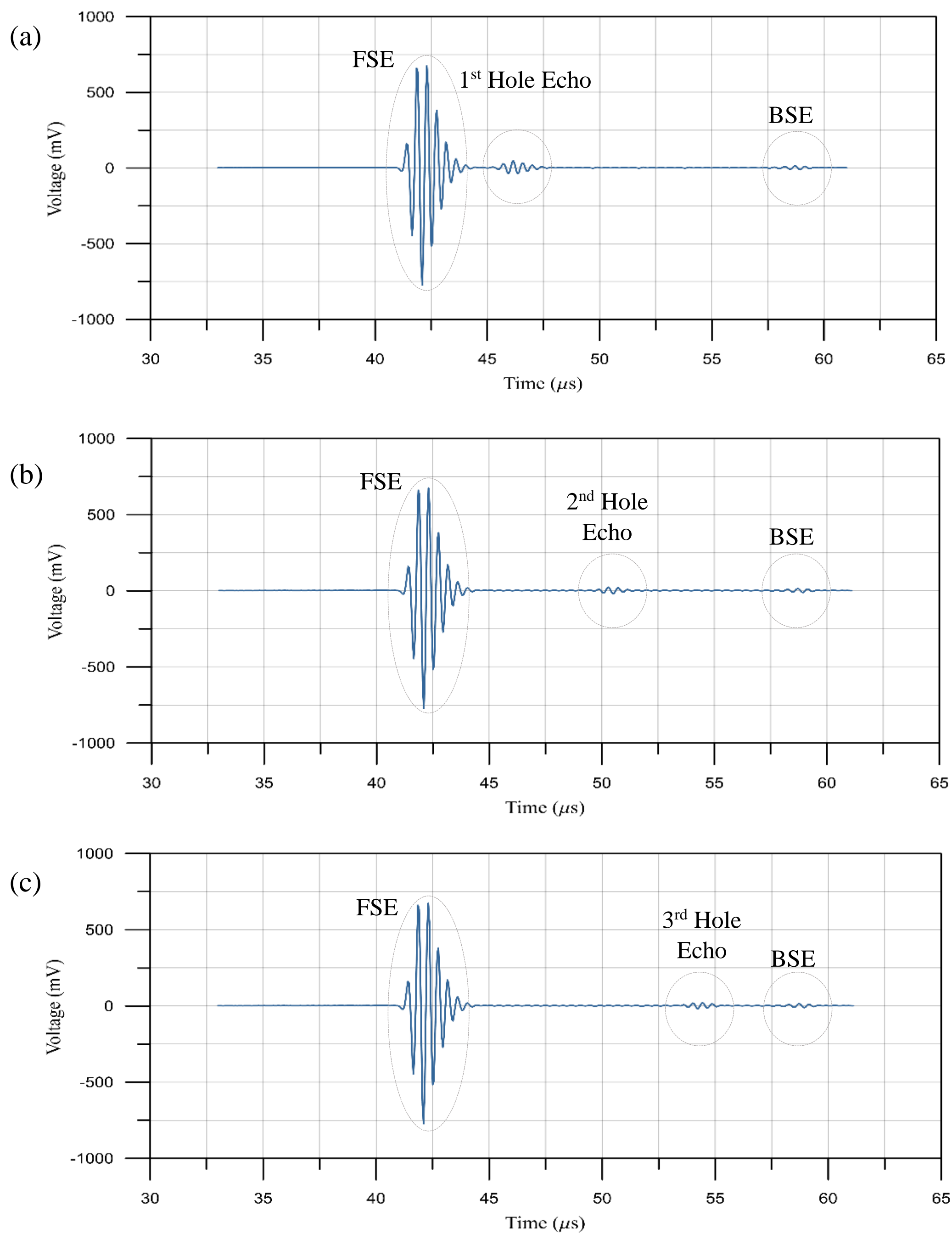

Figure 4.14: Result of the CMUT pulse-echo test of: (a) wall surfaces and 1st hole, (b) wall surfaces and 2nd hole, and (c) wall surfaces and 3rd hole.

Based on the speed of sound of the medium and reflector, 1540 m/s and 6320 m/s, respectively, the round-trip of the ultrasound wave was calculated. Thus, the FS, the first hole (1st Hole), second hole (2nd Hole), third hole (3rd Hole), and the BS echoes of the aluminum block were successfully distinguished.

It is observed from Figure 4.14 that the reflected signals of the flaws are slightly larger than the reflected signals of the back surface. The reason behind that is that due to the small diameter of the CMUT element (3mm) compared to the diameter of the holes (4mm), some amount of ultrasound waves reflect from the flaw and the rest of the ultrasound waves propagate through the flaw toward the back surface of the aluminum block. The amplitudes of the reflected signal are generally large when the tested sample is flawless, as indicated in the Figure 4.13. Additionally, due to CMUT low output pressure, the farther the ultrasound signal travels within the sample, the greater the attenuation; therefore, the weak signals were anticipated.

Chapter 5

Summary and Future Work

5.1 Summary

Throughout the course of this research, analytical modeling, simulation, fabrication and characterization of CMUT have been demonstrated. Geometries and parameters of CMUT are designed to meet the frequencies dedicated for non-destructive testing (NDT) applications. The analytical model, programmed in *Mathematica* software based on the lumped mass model showed that the CMUT's pull-in voltage was 75 V and had in-air and in-immersion center frequencies of 5.51 and 2.26 MHz, respectively. The FEA of CMUT was developed using *COMSOL Multiphysics* to verify the analytical model results. The FEA results indicated that the CMUT had a pull-in voltage of 74.9 and resonated at 5.47 MHz in-air and 2.19 MHz in-immersion. Based on the modeling results, the CMUT was fabricated using wafer bonding process, achieving unique yield and better uniformity. The fabricated CMUT was then tested and characterized to investigate the performance of the ultrasound device. The in-air experimental results showed that the CMUT resonated at 5.51 MHz. In-immersion characterization also revealed that the 2.22 MHz CMUT obtained a -6 dB fractional bandwidth of 189%, and a receive sensitivity of 31.15 mV/kPa. The pulse-echo test performed on an aluminum block in the case of absence and presence of the defects showed success in distinguishing the surfaces and defects of the tested sample.

5.2 Future Work

While more research on CMUTs is still ongoing, the chances in improving the performance of CMUTs are quite possible. The future work should aim to benefit from the features of the CMUTs while solving the issues that CMUTs suffer from. One of the main issues is the output pressure. Due to the fact that CMUTs suffer from low output pressure that leads to a low depth of ultrasound wave penetration, this issue should be addressed. One of the effective methods has been demonstrated by incorporating an annular CMUT with circular PZT probe [11]. This method would likely solve the low output pressure of the CMUT by allocating the PZT transducer as a transmitter and CMUT as a receiver, based on PZT high output pressure and CMUT high receive sensitivity. Thus, achieving enhanced overall sensitivity and improved axial resolution.

A flexible annular CMUT array would be a prime candidate to be considered in future work. The key attribute of the flexible CMUT is that it can be curved to acquire larger imaging volume and concordantly attached to a cylinder-shape probe for small area imaging [56]. Flexible CMUT can be fabricated using adhesive wafer bonding process [57], as depicted in Figure 5.1. The key factor using adhesive wafer bonding process in fabricating the flexible CMUT, underlies in employing Benzocyclobutene (BCB) polymer as an adhesive layer that can enable wafer bonding on flexible materials such as polyimide film [57].

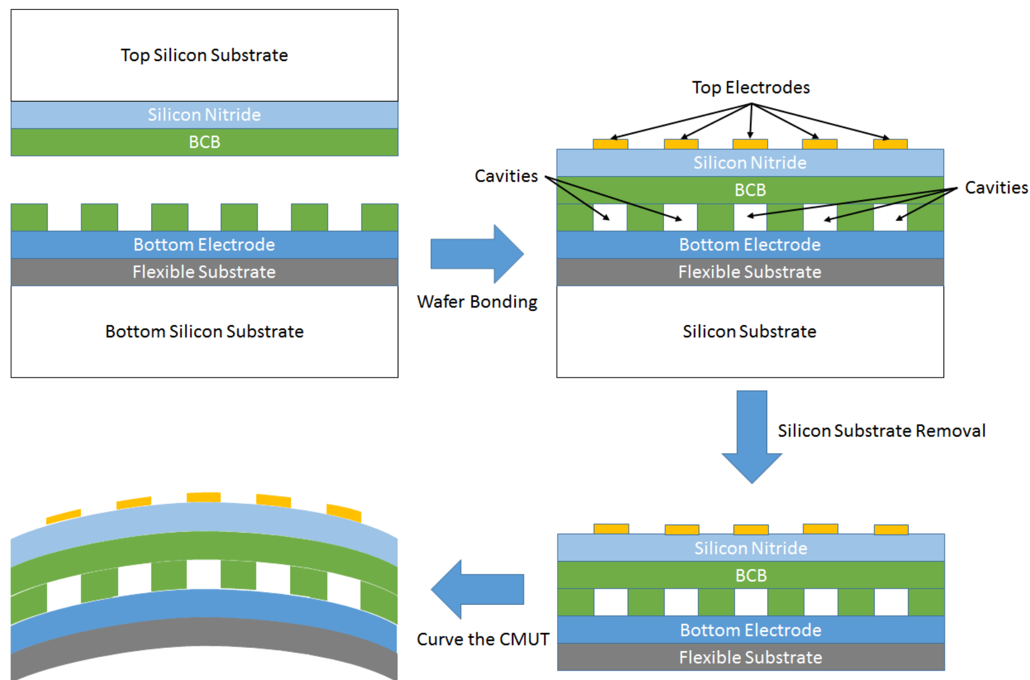

Figure 5.1: Illustration of flexible CMUT fabrication process [57].

After fabricating and characterizing the flexible annular CMUT array, the feasibility of the future work underlies in seamlessly integrating the flexible annular CMUT array with a PZT probe, creating a high performance hybrid ultrasound transducer. Due to the high sensitivity of CMUTs and high output pressure of the PZT transducers, the integrated flexible CMUTs-PZT system would help solving the prime issues of ultrasound transducers for NDT applications such as detection of pipeline cracks and the delamination of aircraft structures. Furthermore, the hybrid ultrasound transducer would also provide a wider fractional bandwidth corresponding to a shorter acoustic pulse and thus a better axial resolution.

Bibliography

[1] Yaralioglu, G. G., Badi, M. H., Ergun, A. S., & Khuri-Yakub, B. T. (2003, October). Improved equivalent circuit and finite element method modeling of capacitive micromachined ultrasonic transducers. In *IEEE Symposium on Ultrasonics, 2003* (Vol. 1, pp. 469-472). IEEE.

[2] Lohfink, A., Eccardt, P. C., Benecke, W., & Meixner, H. (2003, October). Derivation of a 1D CMUT model from FEM results for linear and nonlinear equivalent circuit simulation. In *IEEE Symposium on Ultrasonics, 2003* (Vol. 1, pp. 465-468). IEEE.

[3] Jin, X., Ladabaum, I., Degertekin, F. L., Calmes, S., & Khuri-Yakub, B. T. (1999). Fabrication and characterization of surface micromachined capacitive ultrasonic immersion transducers. *Journal of Microelectromechanical systems*, *8*(1), 100-114.

[4] Huang, Y., Ergun, A. S., Haeggstrom, E., Badi, M. H., & Khuri-Yakub, B. T. (2003). Fabricating capacitive micromachined ultrasonic transducers with wafer-bonding technology. *Journal of microelectromechanical systems*, *12*(2), 128-137.

[5] Khuri-Yakub, B. T., & Oralkan, Ö. (2011). Capacitive micromachined ultrasonic transducers for medical imaging and therapy. *Journal of micromechanics and microengineering*, *21*(5), 054004.

[6] Haller, M. I., & Khuri-Yakub, B. T. (1996). A surface micromachined electrostatic ultrasonic air transducer. *IEEE transactions on ultrasonics, ferroelectrics, and frequency control*, *43*(1), 1-6.

[7] Erguri, A. S., Huang, Y., Zhuang, X., Oralkan, O., Yarahoglu, G. G., & Khuri-Yakub, B. T. (2005). Capacitive micromachined ultrasonic transducers: Fabrication technology. *IEEE transactions on ultrasonics, ferroelectrics, and frequency control*, 52(12), 2242-2258.

[8] Bayram, B., Oralkan, O., Ergun, A. S., Hæggstrom, E., Yaralioglu, G. G., & Khuri-Yakub, B. T. (2005). Capacitive micromachined ultrasonic transducer design for high power transmission. *ieee transactions on ultrasonics, ferroelectrics, and frequency control*, 52(2), 326-339.

[9] Guldiken, R. O., McLean, J., & Degertekin, F. L. (2006). CMUTS with dual electrode structure for improved transmit and receive performance. *IEEE transactions on ultrasonics, ferroelectrics, and frequency control*, 53(2), 483-491.

[10] Huang, Y., Haeggstrom, E. O., Zhuang, X., Ergun, A. S., & Khuri-Yakub, B. T. (2004, August). Optimized membrane configuration improves CMUT performance. In *IEEE Ultrasonics Symposium*, 2004 (Vol. 1, pp. 505-508). IEEE.

[11] Zheng, Z., Na, S., Albert, I., Chen, H., Li, Z., Wong, L. L., ... & Yeow, J. T. (2018). Development of a Novel CMUT-Based Concentric Dual-Element Ultrasonic Transducer: Design, Fabrication, and Characterization. *Journal of Microelectromechanical Systems*, 27(3), 538-546.

[12] Logan, A. S., & Yeow, J. T. (2008, November). 1-D CMUT arrays fabricated using a novel wafer bonding process. In 2008 *IEEE Ultrasonics Symposium* (pp. 1226-1229). IEEE.

[13] Szabo, T. L. (2004). *Diagnostic ultrasound imaging: inside out*. Academic Press.

[14] Blitz, J., & Simpson, G. (1995). *Ultrasonic methods of non-destructive testing* (Vol. 2). Springer Science & Business Media.

[15] Kennedy, J. E. (2005). High-intensity focused ultrasound in the treatment of solid tumours. *Nature reviews cancer*, 5(4), 321.

[16] Kennedy, J. E., Ter Haar, G. R., & Cranston, D. (2003). High intensity focused ultrasound: surgery of the future?. *The British journal of radiology*, 76(909), 590-599.

[17] Graff, K. (1991). Historical overview of ultrasonic test development. *American Society for Nondestructive Testing, Nondestructive Testing Handbook*. Second Edition., 7, 23-32.

[18] BCC Research: New Applications Charging Growth in Ultrasonic Technology Markets in *Entertainment Close Up*, Close-Up Media inc. Jacksonville, USA July 03, 2016.

[19] Reid, J. R. (2001). Dielectric Charge Effect on capacitive MEMS actuator. In IEEE MTT-S *International Microwave Symposium*, RF MEMS Workshop, Phoenix, AZ, 2001.

[20] Huang, Y., Haegstrom, E., Bayram, B., Zhuang, X., Ergun, A. S., Cheng, C. H., & Khuri-Yakub, B. T. (2006). Comparison of conventional and collapsed region operation of capacitive micromachined ultrasonic transducers. *ieee transactions on ultrasonics, ferroelectrics, and frequency control*, 53(10), 1918-1933.

[21] T. L. Szabo, *Diagnostic ultrasound imaging: Inside out*, 2nd ed. Kidlington, Oxford, United Kingdom: Academic Press, 2014.

[22] Behnamfar P, Molavi R, and Mirabbasi S 2017 Transceiver design for CMUT-based super-resolution ultrasound imaging *IEEE Transactions on Biomedical Circuits & Systems*, 10(2), 383-393.

[23] Logan, A. S., Wong, L. L., & Yeow, J. T. (2011). A 1-D capacitive micromachined ultrasonic transducer imaging array fabricated with a silicon-nitride-based fusion process. *IEEE/ASME Transactions on Mechatronics*, 16(5), 861-865.

[24] Yoon H S, Chang C, Jang J H, et al 2016 Ex vivo HIFU experiments using a 32×32 -element CMUT array *IEEE Transactions on Ultrasonics, Ferroelectrics and Frequency Control*, 63(12), 2150-2158.

[25] Frew, S., Najar, H., & Cretu, E. (2009, September). VHDL-AMS behavioural modelling of a CMUT element. In 2009 *IEEE Behavioral Modeling and Simulation Workshop* (pp. 19-24). IEEE.

[26] Bhuyan, A., Choe, J. W., Lee, B. C., Wygant, I., Nikoozadeh, A., Oralkan, O., & Khuri-Yakub, B. T. (2013, February). 3D volumetric ultrasound imaging with a 32× 32 CMUT array integrated with front-end ICs using flip-chip bonding technology. *In 2013 IEEE International Solid-State Circuits Conference Digest of Technical Papers* (pp. 396-397). IEEE.

[27] Onda Corporation, CA, USA, "Table of acoustic properties of material", Available: http://www.ondacorp.com/tecref_acoustictable.

[28] Wygant, I. O., Kupnik, M., & Khuri-Yakub, B. T. (2008, November). Analytically calculating membrane displacement and the equivalent circuit model of a circular CMUT cell. In *2008 IEEE Ultrasonics Symposium* (pp. 2111-2114). IEEE.

[29] Song, S. J., Shin, H. J., & Jang, Y. H. (2002). Development of an ultra sonic phased array system for nondestructive tests of nuclear power plant components. *Nuclear engineering and design*, 214(1-2), 151-161.

[30] Chatillon, S., Cattiaux, G., Serre, M., & Roy, O. (2000). Ultrasonic non-destructive testing of pieces of complex geometry with a flexible phased array transducer. *Ultrasonics*, 38(1-8), 131-134.

[31] Mahaut, S., Roy, O., Beroni, C., & Rotter, B. (2002). Development of phased array techniques to improve characterization of defect located in a component of complex geometry. *Ultrasonics*, 40(1-8), 165-169.

[32] Smith, R. A., Bending, J. M., Jones, L. D., Jarman, T. R., & Lines, D. I. (2003). Rapid ultrasonic inspection of ageing aircraft. *Insight-Non-Destructive Testing and Condition Monitoring*, 45(3), 174-177.

[33] Brotherhood, C. J., Drinkwater, B. W., & Freemantle, R. J. (2003). An ultrasonic wheel-array sensor and its application to aerospace structures. *Insight-Non-Destructive Testing and Condition Monitoring*, 45(11), 729-734.

[34] Jamil, M., Khan, A. M., Hegab, H., Sarfraz, S., Sharma, N., Mia, M., ... & Pruncu, C. I. (2019). Internal cracks and non-metallic inclusions as root causes of casting failure in sugar mill roller shafts. *Materials*, 12(15), 2474.

[35] Oralkan, O., Ergun, A. S., Cheng, C. H., Johnson, J. A., Karaman, M., Lee, T. H., & Khuri-Yakub, B. T. (2003). Volumetric ultrasound imaging using 2-D CMUT arrays. *IEEE transactions on ultrasonics, ferroelectrics, and frequency control*, 50(11), 1581-1594.

[36] Logan, A., & Yeow, J. T. (2009). Fabricating capacitive micromachined ultrasonic transducers with a novel silicon-nitride-based wafer bonding process. *IEEE transactions on ultrasonics, ferroelectrics, and frequency control*, 56(5), 1074-1084.

[37] Thränhardt, M., Eccardt, P. C., Mooshofer, H., Hauptmann, P., & Degertekin, L. (2009, October). A resonant CMUT sensor for fluid applications. In *SENSORS, 2009 IEEE* (pp. 878-883). IEEE.

[38] Khuri-Yakub, B. T., Cheng, C. H., Degertekin, F. L., Ergun, S., Hansen, S., Jin, X. C., & Oralkan, O. (2000). Silicon micromachined ultrasonic transducers. *Japanese Journal of Applied Physics*, 39(5S), 2883.

[39] Cianci, E., Visigalli, L., Foglietti, V., Caliano, G., & Pappalardo, M. (2003). Improvements towards a reliable fabrication process for cMUT. *Microelectronic Engineering*, 67, 602-608.

[40] Ahrens, O., Buhrdorf, A., Hohlfeld, D., Tebje, L., & Binder, J. (2002). Fabrication of gap-optimized CMUT. *IEEE transactions on ultrasonics, ferroelectrics, and frequency control*, 49(9), 1321-1329.

[41] Belgacem, B., Alquier, D., Muralt, P., Baborowski, J., Lucas, S., & Jerisian, R. (2003). Optimization of the fabrication of sealed capacitive transducers using surface micromachining. *Journal of Micromechanics and Microengineering*, 14(2), 299.

[42] Manwar, R. (2017). A BCB Diaphragm Based Adhesive Wafer Bonded CMUT Probe for Biomedical Application.

[43] You, W., Cretu, E., & Rohling, R. (2011). Analytical modeling of CMUTs in coupled electro-mechano-acoustic domains using plate vibration theory. *IEEE Sensors Journal*, 11(9), 2159-2168.

[44] Szabo, T. L. (2004). *Diagnostic ultrasound imaging: inside out*. Academic Press.

[45] Hsu, T. R. (2008). *MEMS and microsystems: design, manufacture, and nanoscale engineering*. John Wiley & Sons.

[46] Ergun, A. S., Yaralioglu, G. G., & Khuri-Yakub, B. T. (2003). Capacitive micromachined ultrasonic transducers: Theory and technology. *Journal of aerospace engineering*, 16(2), 76-84.

[47] Tilmans, H. A. (1996). Equivalent circuit representation of electromechanical transducers: I. Lumped-parameter systems. *Journal of Micromechanics and Microengineering*, 6(1), 157.

[48] Park, K. K. (2011). *Capacitive micromachined ultrasonic transducer (cmut) for chemical detection in air* (Doctoral dissertation, Stanford University).

[49] Wong, L. (2014). Capacitive Micromachined Ultrasonic Transducers for Non-destructive Testing Applications.

[50] Zhuang, X. (2008). *Capacitive micromachined ultrasonic transducers with through-wafer interconnects*. Stanford University.

[51] Anbalagan, S. A., Uma, G., & Umapathy, M. (2006). Modeling and simulation of capacitive micromachined ultrasonic transducer (CMUT). *In Journal of Physics: Conference Series* (Vol. 34, No. 1, p. 595). IOP Publishing.

[52] Park, K. K., Lee, H. J., Crisman, P., Kupnik, M., Oralkan, O., & Khuri-Yakub, B. T. (2008, November). Optimum design of circular CMUT membranes for high quality factor in air. *In 2008 IEEE Ultrasonics Symposium* (pp. 504-507). IEEE.

[53] Bhuyan, A., Choe, J. W., Lee, B. C., Wygant, I., Nikoozadeh, A., Oralkan, O., & Khuri-Yakub, B. T. (2013, February). 3D volumetric ultrasound imaging with a 32× 32 CMUT array integrated with front-end ICs using flip-chip bonding technology. In *2013 IEEE International Solid-State Circuits Conference Digest of Technical Papers* (pp. 396-397). IEEE.

[54] Gurun, G., Hasler, P., & Degertekin, F. L. (2011). Front-end receiver electronics for high-frequency monolithic CMUT-on-CMOS imaging arrays. *IEEE transactions on ultrasonics, ferroelectrics, and frequency control, 58*(8), 1658-1668.

[55] Savoia, A., Caliano, G., Mauti, B., & Pappalardo, M. (2011, October). Performance optimization of a high frequency CMUT probe for medical imaging. In *2011 IEEE International Ultrasonics Symposium* (pp. 600-603). IEEE.

[56] Albert, I., Chen, H., Wong, L. L., Na, S., Li, Z., Macecek, M., & Yeow, J. T. (2016). Fabrication of a curved row–column addressed capacitive micromachined ultrasonic transducer array. *Journal of Microelectromechanical Systems*, 25(4), 675-682.

[57] Li, Z. (2017). Fabrication of capacitive micromachined ultrasonic transducers based on adhesive wafer bonding.

[58] Logan, A. S. (2010). The design, fabrication and characterization of capacitive micromachined ultrasonic transducers for imaging applications.

Appendices

Appendix-Images of CMUT Masking Layouts and Fabricated Devices

(a)

(b)

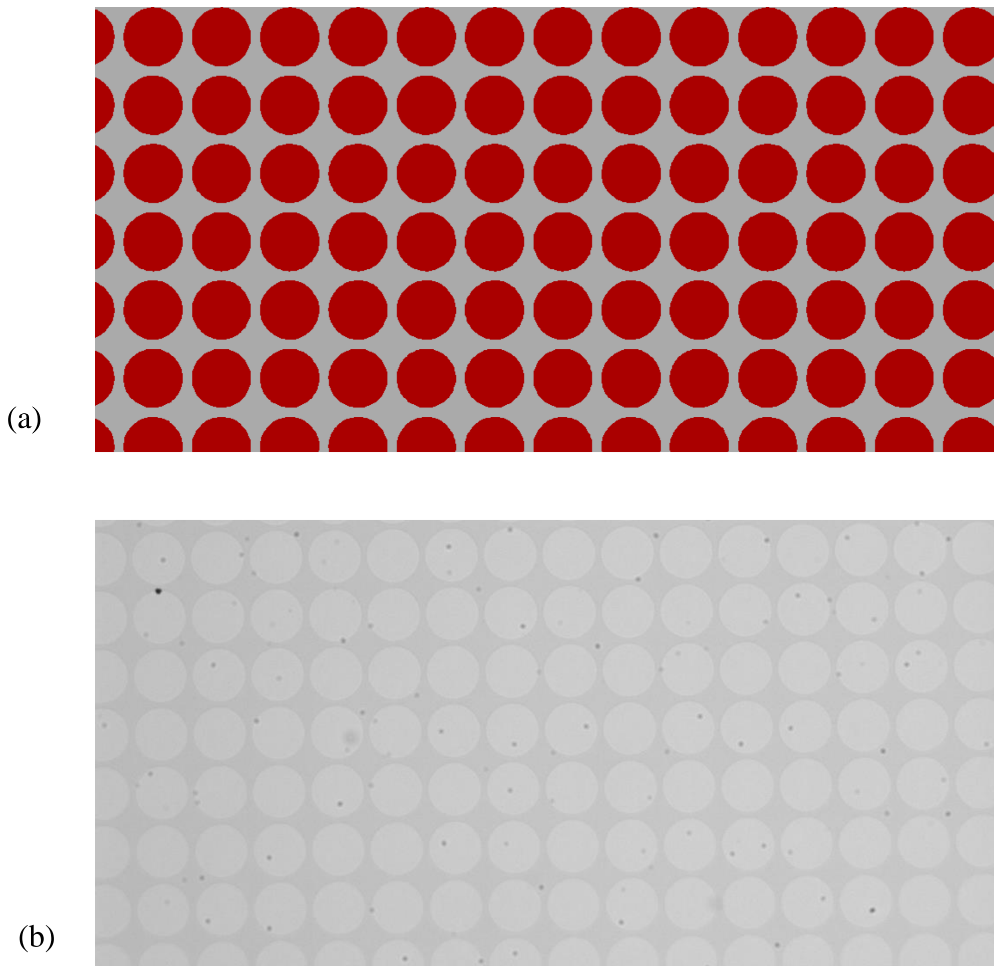

Figure 2: Image of (a) Masking layout of CMUT's cells, and (b) CMUT's cells of the fabricated device.

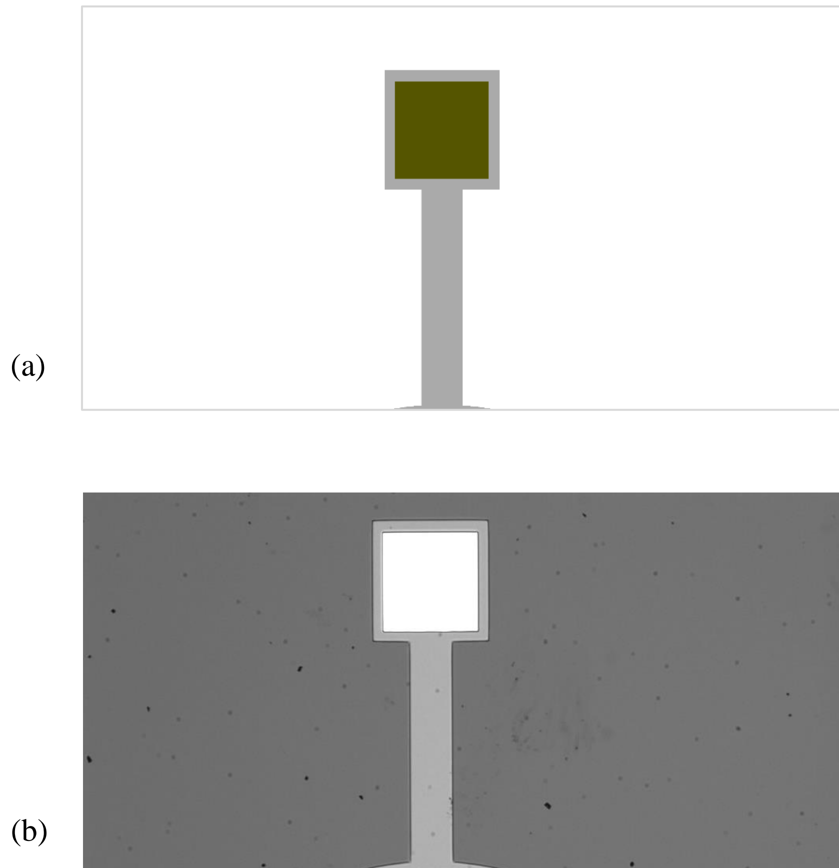

Figure 3: Image of (a) Masking layout of CMUT's top electrode, and (b) Top electrode of the fabricated device.

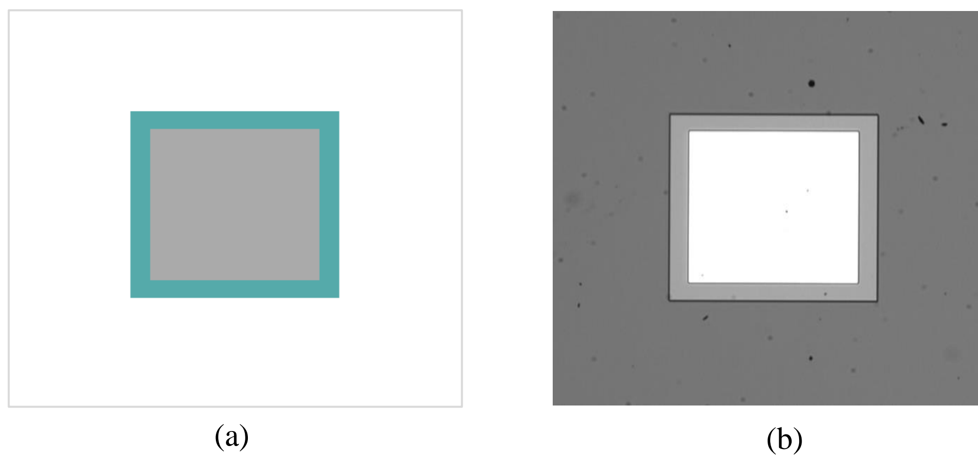

Figure 4: Image of (a) Masking layout of CMUT's bottom electrode, and (b) Bottom electrode of the fabricated device.

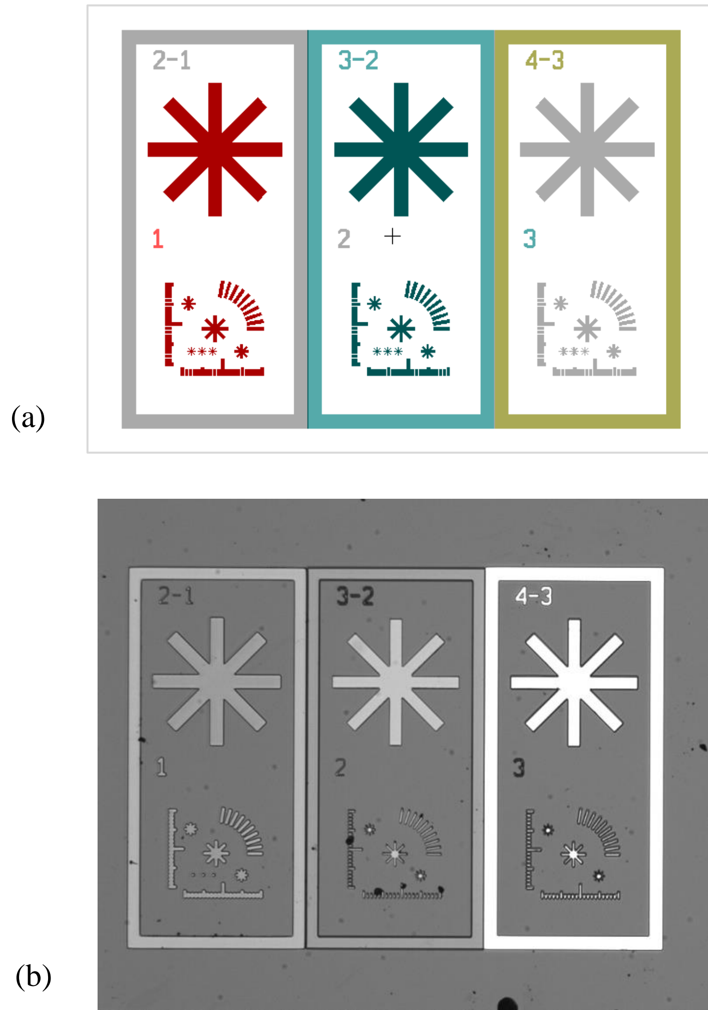

Figure 5: Image of (a) Masking layout of CMUT's alignment marks, and (b) Alignment marks of the fabricated device.